On constraining 3D seismic anisotropy in subduction, mid-ocean-ridge, and plume environments with teleseismic body wave data

Manuele Faccenda [*], Brandon P. VanderBeek

Dipartimento di Geoscienze, Università di Padova, via Gradenigo 6, 35131 Padova, Italy

ARTICLE INFO

ABSTRACT

Conventional seismic tomography studies consider the Earth's interior as mechanically isotropic, despite seismic anisotropy being widely observed. This current standard approach to seismic imaging is likely to lead to significant artefacts in tomographic images with first-order effects on interpretations and hinders the quantitative integration of seismology with geodynamic flow models. Although a few methodologies have been proposed for carrying out anisotropic tomography, their ability in simultaneously recovering isotropic and anisotropic structures has not been rigorously tested. In this contribution we use geodynamic and seismological modeling to predict the elastic properties and synthetic teleseismic P- and S-wave travel-time datasets for three different tectonic settings: a plume rising in an intraplate setting, a divergent margin, and a subduction zone. Subsequently, we perform seismic anisotropy tomography testing a recently developed methodology that allows for the inversion of an arbitrarily oriented weakly anisotropic hexagonally symmetric medium using multiple body-wave datasets. The tomography experiments indicate that anisotropic inversions of separate and joint P- and S-wave travel-times are capable of recovering the first order isotropic velocity anomalies and anisotropic patterns. In particular, joint P- and S-wave anisotropic inversions show that by leveraging both phases it is possible to greatly mitigate issues related to imperfect data coverage common in seismology and reduce parameter trade-offs. In contrast, by neglecting seismic anisotropy, isotropic tomographic models provide no information on the mantle fabrics and in all cases are contaminated by strong velocity artifacts. In the inversions the magnitude of anisotropy (as well as that of seismic anomalies) is always underestimated owing to regularization procedures and smearing effects. It follows that the true seismic anisotropy of mantle rocks is likely higher than estimated from anisotropic tomographies, and more consistent with predictions from laboratory and numerical micromechanical experiments. Altogether, these results suggest that anisotropic body-wave tomography could provide unprecedented information about the Earth's deep geological structure, and that the latter could be better recovered by complementing teleseismic body-wave travel-times with other geophysical datasets.

1. Introduction

One of the principal objectives of Earth science is to understand the internal dynamics, structure and composition of our planet. Because most the Earth is inaccessible to direct investigation, indirect methods, such as seismological methods, and geodynamic modelling are often used to generate a window through which to explore the Earth's interior.

On the one hand, geodynamic models give insights into the complex dynamical behaviour of the Earth, where several thermomechanical and petrological processes occur simultaneously at geological timescales. Nowadays, thanks to the enormously increased computational power, three-dimensional simulations of mantle convection coupled with petrological databases provide a realistic estimate of the tectono-magmatic evolution of the Earth, with results that are often compatible with the available geological and geophysical data (e.g., Katz et al., 2007; Burov and Gerya, 2014; Colli et al., 2016). Additionally, over the last few years, coupled micro-macro geodynamic modelling has enabled linking such tectono-magmatic evolution with the development of elastic anisotropy in specific tectonic settings (e.g., Faccenda and Capitanio, 2013; Ito et al., 2014; Hedjazian et al., 2017; Hu et al., 2017; Zhou et al., 2018; Lo Bue et al., 2021), providing new ways to couple models to observations.

On the other hand, seismological methods are by far the best instrument for studying the Earth's current deep structure and physical

---

properties. In particular, seismic tomography is a technique that allows mapping the lateral variations of the elastic properties (particularly wave-propagation velocity) of the Earth's interior from seismic travel time and waveform data. Potential sources for seismic velocity anomalies imaged by tomography are (i) temperature anomalies, compositional variations and solid-solid or solid-fluid phase transitions (herein named altogether thermo-petrological anomalies), and (ii) mechanical anisotropy generated by the Lattice Preferred Orientation (LPO) of intrinsically anisotropic crystals or by the Shape Preferred Orientation (SPO) of fine-layered isotropic structures (e.g., Babuška and Cara, 1991; Nolet et al., 2007). Seismic anisotropy is widely observed at different levels of the mantle, and is mostly concentrated at boundary layers (lithosphere, asthenosphere, transition zone, core-mantle boundary; Montagner, 1998; Long and Becker, 2010; Tommasi and Vauchez, 2015) and around sliding rigid plates inducing relatively high-stress deformation in the surrounding mantle (McNamara et al., 2002; Faccenda and Capitanio, 2013; Faccenda, 2014; Chang et al., 2016; Sturgeon et al., 2019).

While studies have emphasized the need to consider anisotropy when tomographically imaging the mantle (e.g., Gresillaud and Cara, 1996; Wu and Lees, 1999; Bokelmann, 2002; Schulte-Pelkum and Blackman, 2003; Sieminski et al., 2007), isotropic tomographic methods are still widely used. Low velocity anomalies are systematically interpreted as indicating a hot and/or volatile rich and/or partially molten mantle. Conversely, high velocity anomalies are thought to represent a cold and/or dry and/or solid mantle. However, over the past decade coupled geodynamic and seismological modeling experiments have indicated that isotropic tomographies could be likely contaminated by velocity artifacts resulting from the unaccounted-for seismic anisotropy (Bezada et al., 2016; VanderBeek and Faccenda, 2021; Eddy et al., 2022; VanderBeek et al., 2023). The magnitude of these artifacts is comparable to those produced by thermo-petrological processes, and thus can strongly bias our understanding of the Earth's internal structure and dynamics. Because tomographic models represent the major probe to the Earth's interior current state, it is fundamental to assess their validity and robustness in order to have a reliable window of the Earth's interior. In addition, it is well established that seismic anisotropy can provide important insights about mantle processes, such as solid-state viscous flow and fluids/magma migration patterns (e.g., Babuška and Cara, 1991; Long and Becker, 2010). Clearly, a seismological approach capable of taking into account seismic anisotropy is desired.

Seismic anisotropy tomography, in which the inverted delay times are decomposed into isotropic and anisotropic components, is a promising methodology. Because body-waves have a better spatial resolution relative to surface waves, several studies have initially proposed a methodology to carry out azimuthal and/or radial anisotropy tomography using P- and/or S-wave travel-times and/or S-wave splitting parameters (e.g., Eberhart-Phillips and Reyners, 2009; Wang and Zhao, 2013; Zhao et al., 2016, 2023). The methodology has been further extended to the inversion of an arbitrarily oriented weakly anisotropic hexagonally symmetric medium (Plomerová and Babuška, 2010; Plomerová et al., 2012; Munzarová et al., 2018; Wang and Zhao, 2021; VanderBeek and Faccenda, 2021). In particular, (VanderBeek and Faccenda, 2021) and (VanderBeek et al., 2023) derived a new body-wave velocity parameterization that, for the first time, (i) allows to invert for arbitrarily oriented hexagonal anisotropy applicable to both separate and joint P- and S-wave datasets, and (ii) largely avoids issues related to the convergence of the non-linear inverse problem and to the starting model-dependence. The velocity parametrization has been tested on realistic 3D model of convergent margins and successfully applied to P-wave teleseismic anisotropic tomography of the Mediterranean basin to yield geodynamically-relevant constraints on mantle fabrics (Rappisi et al., 2022).

In this contribution, we further test this recently developed inversion strategy against two other geodynamically-derived and relevant tectonic settings, i.e., a divergent margin and an intraplate setting with a plume

rising from the base of the mantle transition zone. In addition, for the first time we present joint P- and S-wave travel-time inversions on all the three types of tectonic settings. To be consistent with the previous studies, and considering that local deep seismicity is scarce if not absent in many tectonic settings, we only employ teleseismic body wave datasets.

2. Methods

2.1. Large-scale geodynamic modeling

The regional scale, thermo-mechanical 3D evolution of (i) an intra-plate tectonic setting with a thermal plume rising and spreading beneath the lithosphere, (ii) a divergent margin characterized by an oceanic spreading ridge, and (iii) a convergent margin with a subducting oceanic plate, has been simulated with I3MG (Gerya, 2019) (Fig. 1). The original software has been modified to account for the distortion of the orthogonal grid in spherical coordinates (see Supplementary Information section S.1.1). All models are symmetric with respect to the equatorial plane, and as such only the portion located in the northern hemisphere is modelled. The rheological model accounts for visco-plastic deformation (see Supplementary Information section S1.2 and model parameters listed in Table S1). Viscous behavior results from combined low-T (Peierls) and high-T (diffusion and dislocation) creep mechanisms according to the flow law parameters shown in (Katayama and Karato, 2008) and (Karato and Wu, 1993). Density, effective heat capacity and effective thermal expansion are computed as a function of the local P-T conditions according to lookup tables generated with the software PERPLE_X for a pyrolytic mantle composition (Mishin et al., 2008). Thus, phase transitions are taken into account self-consistently in our models. The oceanic crust is absent in the spreading ridge and rising plume models as it is not relevant for their tectonic evolution. Melting reactions are not modeled, which results in a strong simplification of the situation likely found below ridge axes, hot spots and volcanic arcs.

The thermal structure of all models is defined by (i) a constant temperature at the top (273 K) and bottom boundaries, (ii) insulating vertical boundaries, (iii) an upper, 90 km thick layer where the conductive geotherm is computed with the Half-Space Cooling Model (Turcotte and Schubert, 2014), (iv) a deeper convective portion of the mantle characterized by $T_{potential} = 1623$ K and an adiabatic gradient of 0.5 K/km. Free slip is imposed on all closed boundaries, while external free slip is applied for permeable boundaries (Gerya, 2019).

Rising of a thermal plume from the bottom of the mantle transition zone has been modeled with a numerical domain ranging $(\phi, r, \theta) = (80–100°, 5731–6371$ km$, 80–90°)$ and discretized with $197 \times 149 \times 101$ nodes (Fig. 1A). An 80 Myr old plate is set at the surface, while the bottom boundary is permeable and with a constant temperature of 1943 K. Rising of hot, buoyant material is triggered by defining an axi-symmetric temperature anomaly at the bottom permeable boundary (e.g., Ito et al., 2014).

In the oceanic spreading ridge model, the numerical domain ranges $(\phi, r, \theta) = (80–100°, 5711–6371$ km$, 80–90°)$ and it has been discretized with $197 \times 165 \times 101$ nodes (Fig. 1C). The ridge structure does not vary along colatitude. The two plates spread apart at a constant rate of 2 cm/yr, with the Euler pole of rotation set at the north pole. The plates age progressively increases from 1 kyr at the ridge axis ($\phi = 90°$) to 40 Myr at the east and west boundaries. The temperature at the bottom boundary is 1953 K, and the east and west vertical boundaries are permeable to longitudinal flow.

For the oceanic plate subduction model, the numerical domain ranges $(\phi, r, \theta) = (60–120°, 5371–6371$ km$, 60–90°)$ and it has been discretized with $293 \times 197 \times 69$ nodes (Fig. 1D). The larger numerical domain is required to model plate subduction and retreat (via the establishment of lateral toroidal flow fields), and its interaction with the uppermost lower mantle. The horizontal portion of the subducting plate is defined $(\phi, \theta) = (85.4–118°, 80–90°)$. The plate age varies from 80 to
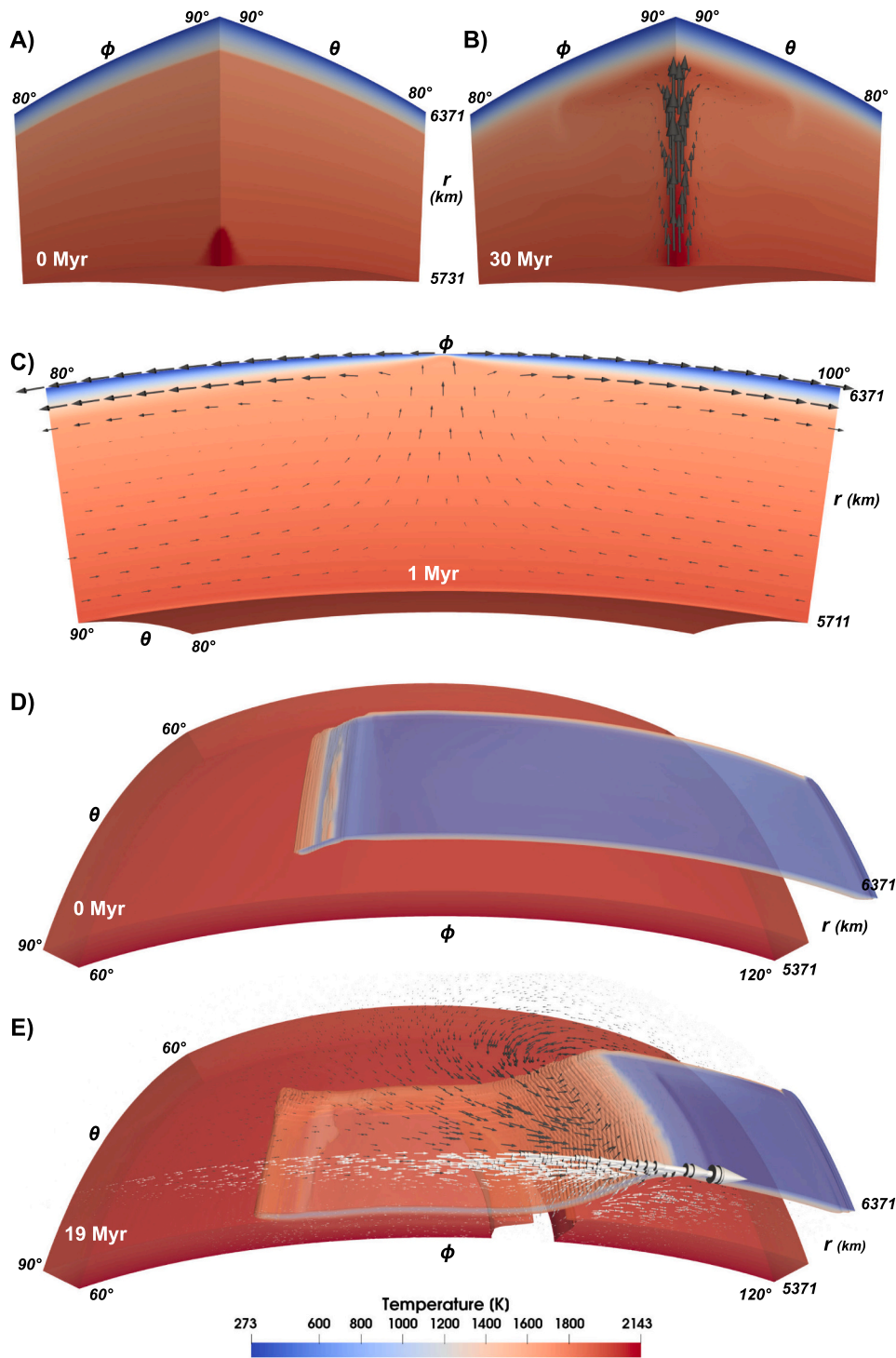
Fig. 1. Temperature and velocity (arrows) fields for the three modeled tectonic settings as predicted by macro-scale geodynamic modeling. (A, B) Rising plume model initial setup and after 30 Myr. Only half of the computational domain (ϕ = 80–90°) is shown. The thermal anomaly is delimited by a 2D gaussian surface containing material at 2143 K, resulting in a 200–250 K temperature anomaly over the mantle transition zone. The 2D gaussian surface is centered at (ϕ, θ) = (90°, 90°), and has a radial extent of 1°, a horizontal standard deviation of 0.4° and a maximum amplitude of 100 km. (C) Oceanic spreading ridge model after 1 Myr. The arrows length at the surface is proportional to the imposed 2 cm/yr divergence rate. (D, E) Oceanic plate subduction model initial setup and after 19 Myr. The opaque surfaces enclose material with viscosity $\geq 10^{21}$ Pa s and are colored according to temperature. In (E) the white (dark grey) arrows indicate the poloidal (toroidal) component of the velocity field. The arrows length in (B) and (E) is downscaled by 10 and 4 times with respect to that in (C).

40 Myr moving from the centre to the plate side, which favors the formation of a curved trench (Morra et al., 2006), and linearly decreases to 1 Myr at (ϕ) = (118–119°) to prevent subduction at the rear. The background plate age is set to 1 Myr to minimize mechanical interaction with and favor subduction of the old plate. The temperature at the bottom boundary is 2123 K. Self-consistent subduction is initially triggered by the imposed 200 km long slab portion (Fig. 1D) and lubricated by a 15 km thick crustal layer with weak brittle behavior. The viscosity of the lower mantle is increased by a factor 30, which favors slab stagnation in the mantle transition zone.

2.2. Micro-scale geodynamic modeling

Knowing the velocity $\vec{v}$, pressure P and temperature T fields of each modeled tectonic setting, mantle fabrics and elastic properties are estimated with the software package ECOMAN (Faccenda et al., 2021) which includes D-REX_M, a modified version of the software D-REX (Kaminski et al., 2004) that (i) accounts for time-dependent, 3D deformation history, (ii) includes crystal aggregates representative of the whole mantle, and (iii) scales the elastic moduli by the local P-T conditions (Faccenda and Capitanio, 2012, 2013; Faccenda, 2014). Mantle fabrics are only computed for the upper mantle, (thus the mantle transition zone is assumed to be elastically isotropic), and only considering the fraction of deformation accommodated by dislocation creep $Fd = \eta_{ductile}/\eta_{disl}$. All crystal aggregates are composed by two mineral phases (Ol:Opx = 70:30, Wd:Grt = 60:40, Rw:Grt = 60:40), each of which is initially represented by 512 randomly distributed crystals. We use standard D-REX parameters (M^* = 10; χ = 0.3; λ^* = 5; normalized Critical Resolved Shear Stress: nCRSS$_{[100](010)}$ = 1, nCRSS$_{[100](001)}$ = 2, nCRSS$_{[001](010)}$ = 3) as calibrated by (Boneh et al., 2015, G3) against high-strain laboratory experiments, resulting in mostly A-type upper mantle fabrics with a dominant hexagonal anisotropic component and a fast symmetry axis. Randomization of upper mantle crystal aggregates is imposed when transforming into upper mantle transition zone aggregates. The crystal aggregates are first advected backward in time, and subsequently advected forward during which strain-induced lattice-preferred-orientation (LPO) is computed. As a result, the final distribution of the aggregates is uniform with a 10 km spacing along each direction.

The aggregate elastic tensor of each crystal aggregates is computed as a function of the crystal orientation, volume fraction, mineral phase modal abundance and local P-T conditions. For the isotropic component of the elastic tensor we use the bulk and shear moduli from lookup tables computed with MMA-EoS (Chust et al., 2017) using the (Stixrude and Lithgow-Bertelloni, 2011) thermodynamic database, which provide a more continuous definition across phase transitions. The remaining anisotropic component is computed using pressure and temperature derivatives of the single crystal elastic moduli as defined in (Faccenda, 2014). The resulting elastic tensors are then reflected with respect to the equatorial plane, yielding a doubled elastic domain ranging $\theta = 80{-}100°$ for the rising plume and divergent margin models, or $\theta = 60{-}120°$ for the convergent margin model.

2.3. Seismological modeling

The methodology for generating synthetic P- and S-waves travel-times and their separate inversion is described in detail in, respectively, (Vanderbeek and Faccenda, 2021) and (Vanderbeek et al., 2023). Here we provide a concise explanation of the employed strategy and in addition describe how the joint P- and S-wave inversions are performed.

2.3.1. Forward problem and synthetic seismic datasets

In each model we set a virtual grid of seismic stations equally spaced 75 km apart (resulting in 21 × 34 = 714 stations for the subduction model and 21 × 21 = 441 stations for the other two tectonic settings; a station density comparable to the USArray) and compute synthetic P- and S-wave travel-times for 54 events placed at 50°–70°–90° angular distances, 20° azimuthal spacing, and 50 km depth (Fig. 2). The dominant period of the waveforms is 10 s and all S-waves have an initial polarization angle of $\zeta = 60°$ measured with respect to Q-axis in a ray-aligned QTL coordinate system. Frequency-dependent anisotropic travel-times are predicted using the heuristic finite-frequency kernels (HFFKs) described by VanderBeek and Faccenda (2021) and Vander-Beek et al. (2023) and verified against delay times measured from full-waveform synthetic seismograms. This approximation extends the 1D paraxial Born kernels of (Dahlen et al., 2000) to anisotropic media by

making the velocity of a scatterer a function of the incoming ray orientation and, in the case of S-waves, the polarisation angle. In this case, an anisotropic finite-frequency travel-time can be approximated as:

$$t = t_{1D} + \int_V (u - u_{1D}) K dV \tag{1}$$

where t_{1D} is the travel-time predicted through a reference 1-D slowness (i.e., the inverse of velocity) model defined by u_{1D}; u is the true 3D slowness in the direction of wave propagation and K is the slowness sensitivity kernel over the volume V. To simplify the computation of K, we use the following approximation for the kernel's cross-sectional shape within the first Fresnel zone proposed by (Schmandt and Humphreys, 2010) and neglect the rapidly diminishing sensitivity outside this region:

$$K(x, r_n) = \frac{Q}{\pi R_f^2(x)} \sin\left(\pi \frac{r_n^2}{R_f^2(x)}\right) \tag{2}$$

where x is the along-ray distance; r_n is the ray-normal distance and R_f is the radius of the first Fresnel volume and the constant Q is a scaling factor defined such that the volume integral over K is equal to the total ray length. Ray paths and 1D travel-times required to evaluate Eqs. 1 and 2 are computed using the TauP Toolkit (Crotwell et al., 1999) and the AK135 velocity model (Kennett et al., 1995).

The propagation slowness used in the construction of the synthetic travel-time datasets are computed from the full elastic tensors via the Christoffel equations. To test the capabilities and limitations of our inversion methodology for different simplifying assumptions of the elastic geodynamic models, three different synthetic seismic datasets (t_{IJ}, t_{HEX} and t_{ISO}) have been generated using:

1. $\mathbf{C_{IJ}}$: the original full elastic tensor field defined by 21 independent elastic moduli;
2. $\mathbf{C_{HEX}}$: an elastic tensor field with hexagonal symmetry defined by 5 independent elastic moduli and that has been generated by filtering $\mathbf{C_{IJ}}$ with tensor decomposition (Browaeys and Chevrot, 2004);
3. $\mathbf{C_{ISO}}$: an isotropic elastic tensor field defined by 2 independent elastic moduli derived from $\mathbf{C_{IJ}}$.

The forward model is discretized using a regular grid with 10 km node spacing in each direction. The grid is centred at $(\phi, \theta) = (90°, 90°)$ and has dimensions of 2000 × 660 × 2000 km for the rising plume and spreading ridge models, while for the subduction model $(\phi, \theta) = (101.5°, 90°)$ and dimensions are 2000 × 700 × 3000 km.

Travel-times are modeled using the discretized form of Eq. 1:

$$t_{P,S} = t_{1D} + \sum_{j=1}^{M} K_j \Delta u_{P,S} \tag{3a}$$

where K_j is the discretized travel-time sensitivity kernel for perturbations to P or S propagation slowness ($\Delta u_{P,S} = u_{P,S} - u_{1D}$). Propagation slownesses are computed directly from the elastic tensor (by solving the Christoffel equations for the $\mathbf{C_{IJ}}$ and $\mathbf{C_{HEX}}$ cases), and using the AK135 velocity model (Kennett et al., 1995) outside the grid net. Note that the propagation slowness depends on the properties of the anisotropic model and the orientation and polarization of the incoming wavefront. In the case of P-waves, a single anisotropic velocity for a given propagation direction exists while for S-waves there are generally two velocities for the qS'- and qS"-polarized waves. Revisiting early work concerning shear wave splitting (e.g., Vinnik et al., 1989; Silver and Chan, 1991), (VanderBeek et al., 2023; Section 3.1) show that the slowness at which the S-wave observed in the principal polarisation direction propagates can be approximated as,

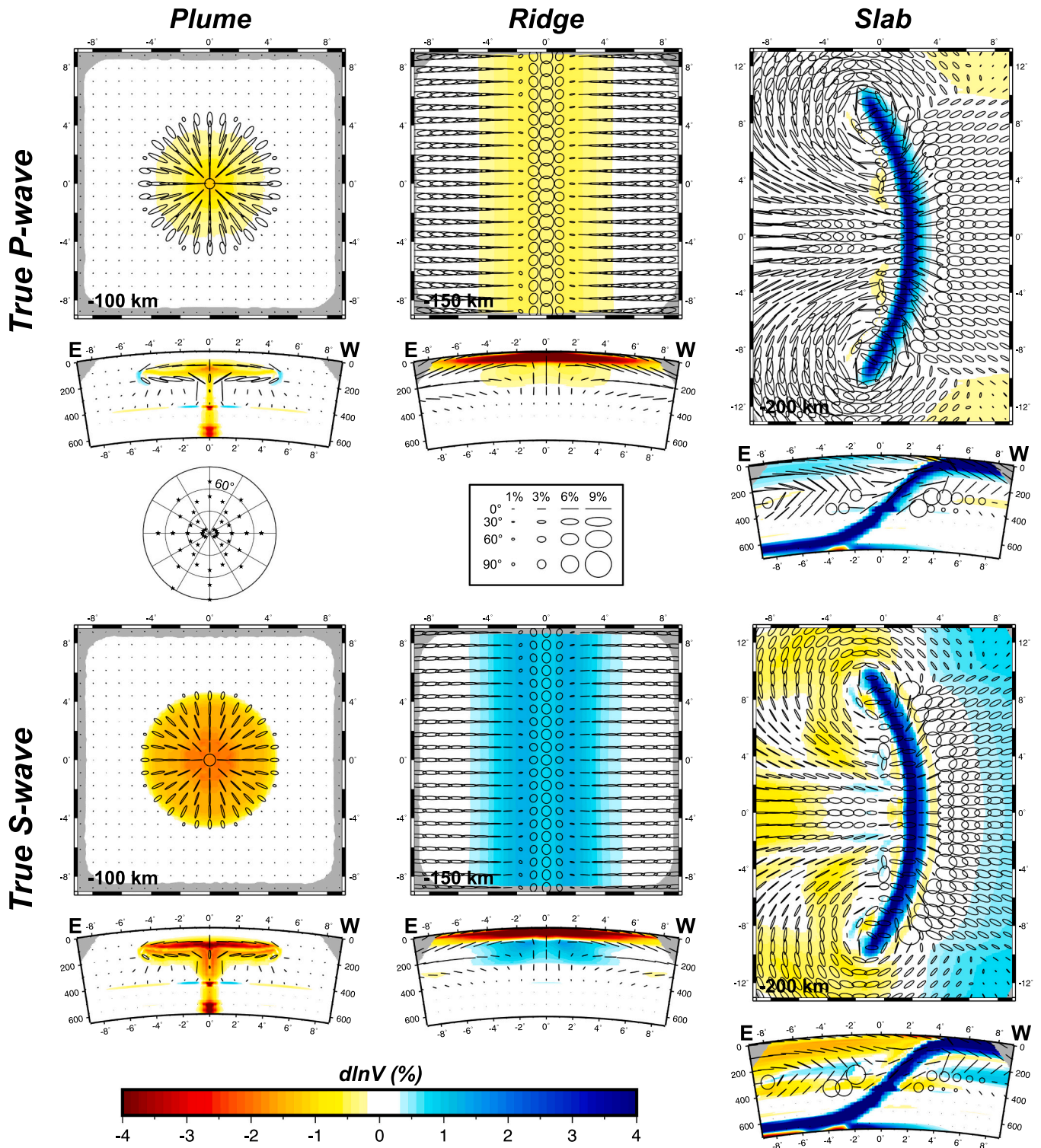$$u_s = u''_s + (u'_s - u'_s)\cos^2(\beta) \tag{3b}$$

Fig. 2. True P-wave (top two panels) and S-wave isotropic anomalies and fast symmetry axis orientations for the three modeled tectonic settings as predicted by micro-scale geodynamics modeling. Horizontal and E-W vertical cross sections (along the equatorial plane of the geodynamic model spherical domain) are shown. Velocity anomalies $\Delta \ln V_{P,S}$ are computed (i) using the average of the three principal velocities, that for an hexagonally symmetric medium with a fast symmetry axis are $V_{fast}, V_{slow}, V_{slow}$, and (ii) with respect to reference radial velocity profiles taken at the corner of the computational domain with minimum the X-Z axes coordinates, which is representative of the far-field, unperturbed mantle. The P-wave low velocity and S-wave high velocity anomalies at 150 km in the ridge model, and the P-wave high velocity and S-wave low velocity anomalies in the subduction model mantle wedge, are caused by deviations from the hexagonally symmetry model. The length of the ellipses major axis is proportional to: $2f(\%) = \frac{\left(V_{fast} - V_{slow}\right)}{\left(V_{fast} + V_{slow}\right)} * 200\%$. The orientation of the fast symmetry axis is parallel to the major axis of the ellipses, while the length of minor axis is proportional to the dip relative to the cross section.

where $u_s^{'}$ and $u_s^{''}$ are the shear wave slownesses for the waves polarised in the plane containing the symmetry axis, qS' (e.g., the fast-direction for an olivine A-type fabric), and orthogonal to this plane, qS'', found by solving the Christoffel equation; β is the angle between incoming shear wave polarization direction and symmetry axis projected into the ray-normal QT-plane. Provided that the delay time between fast- and slow-polarised shear waves remains less than ~T/5 where T is the dominant period, Equation 3 is valid and the incoming shear wave is well-approximated by a single polarisation angle (VanderBeek et al., 2023; Chevrot et al., 2004; Rümpker and Silver, 1998).

2.3.2. Inverse problem

For the inversions, we assume a weakly anisotropic hexagonally symmetric media which is a good approximation of the Earth's upper mantle (Becker et al., 2006). Under this assumption, the quasi-P and quasi-S velocities are well-approximated by functions of the form (e.g., Thomsen, 1986):

$$u_P = \overline{u}_P [1 + f_P \cos(2\alpha)]^{-1}, \tag{4a}$$

$$u_S^{'} = \overline{u}_S \frac{(1 + f^{'})}{(1 + f^{'})} \left[1 + f_S^{'} \cos(4\alpha)\right]^{-1}, \tag{4b}$$

$$u_S^{''} = \overline{u}_S \left[1 + f_S^{''} \cos(2\alpha)\right]^{-1} \tag{4c}$$

where $\overline{u}_P$ and $\overline{u}_S$ are the mean P- and S-wave ($u_s^{'}$) slowness; f_P, $f_S^{'}$, and $f_S^{''}$ are the anisotropic fractions that define the amplitude of the directional velocity variations of the qP, $qS^{'}$- and $qS^{''}$-polarised waves and can be positive (fast symmetry axis) or negative (slow symmetry axis) depending on the particular cause of anisotropy in the medium; here we assume a fast-symmetry axis appropriate for common olivine-dominated mantle mineral fabrics. The angle α is related to the dot-product between the ray and symmetry axis unit vectors,

$$\cos(\alpha) = [\cos(\phi - \psi)\cos(\theta)\cos(\gamma) + \sin(\theta)\sin(\gamma)] \tag{5}$$

where ϕ and θ are the azimuth and elevation of the ray path and ψ and γ are the azimuth and elevation of the hexagonal symmetry axis. The inversion is then parametrized following (VanderBeek and Faccenda, 2021; VanderBeek et al., 2023) using the mean slowness ($\overline{u}_P$ and/or $\overline{u}_S$) and the three anisotropic variables:

$$A = |f_p| \cos^2(\gamma) \cos(2\psi) \tag{6a}$$

$$B = |f_p| \cos^2(\gamma) \sin(2\psi) \tag{6b}$$

$$C = \sqrt{|f_p|} \sin(\gamma) \tag{6c}$$

The anisotropic parameters can then be recovered as $f_P = G + C^2$, $\psi = \arctan\left[\frac{B}{G+A}\right]$, and $\gamma = \arctan\left[C/\sqrt{G}\right]$, where $G = \sqrt{A^2 + B^2}$. Considering the strong correlation between f_p, $f_s^{'}$, and $f_s^{'}$ (Becker et al., 2006), we assume the following fixed anisotropic ratios, $\frac{f_s^{'}}{f_p} = -0.273$ and $\frac{f_s^{'}}{f_p} = 0.657$ based on inspection of the geodynamic model elastic properties. This allows us to parameterise anisotropy solely in terms of the P-wave anisotropic fraction. For independent P and S travel-time inversions, the perturbation vector then consists of four sets of parameters, $\Delta m = [\Delta \overline{u}; \Delta A; \Delta B; \Delta C]$. These parameters are discretised using a regular grid with same dimensions as those of the forward model grids but 40 km node spacing along each directions, resulting in $51 \times 19 \times 76$ (subduction model) and $51 \times 18 \times 51$ nodes (spreading ridge ad rising plume models). Joint inversions, simply require adding an additional slowness parameter such that there is one for both $\overline{u}_P$ and $\overline{u}_S$. This parametrisation has the advantage that (i) it allows to invert for arbitrarily oriented hexagonal anisotropy applicable to both P- and S-wave propagation, and (ii) it largely avoids issues related to the convergence of the

non-linear anisotropic inverse problem and starting model-dependence.

We use an iterative Gauss-Newton method to minimise a least-squares objective function of the form (e.g., Tarantola and Valette, 1982; Aster et al., 2018):

$$\vartheta = res(m, \Delta m) C_d^{-1} res(m, \Delta m) + \epsilon^2 \Delta m^T C_m^{-1} \Delta m + \lambda^2 (L \Delta m)^T (L \Delta m) \tag{7}$$

where res is a (N x 1) vector of data residuals which is a non-linear function of the starting model, m, and the (M x 1) cumulative model perturbation vector, Δm; C_d is the (N x N) data covariance matrix which we assume to be diagonal and composed of the squared data uncertainties; C_m is the (M x M) model covariance matrix; L is an (M x M) matrix that defines the finite difference 3D Laplacian operator that constrains Δm to be spatially smooth; lastly $\in$ and λ are Lagrangian multipliers that limit the size and roughness of the model perturbation vector. The last two terms in Eq. 7 are required to regularise the otherwise under-determined and ill-posed inverse problem.

To minimize Eq. 7, we use the LSQR algorithm (Paige and Saunders, 1982) to iteratively solve the following system of equations linearised about the current model:

$$\begin{bmatrix} C_d^{-\frac{1}{2}} J \\ \epsilon_u C_u^{-\frac{1}{2}} \\ \epsilon_a C_a^{-\frac{1}{2}} \\ \epsilon_a D_f \\ \lambda_u L_u \\ \lambda_a L_a \end{bmatrix} \delta m = \begin{bmatrix} C_d^{-\frac{1}{2}} res \\ -\epsilon_u C_u^{-\frac{1}{2}} \Delta m_{l-1} \\ 0 \\ \epsilon_a D_f \Delta m_{l-1} \\ 0 \\ 0 \end{bmatrix} \tag{8}$$

where $\delta m = [\delta u; \delta A; \delta B; \delta C]$ are the incremental parameter changes added to the cumulative model perturbations from the previous iteration, Δm_{l-1}. The (N x M) matrix J is the data Jacobian obtained by differentiating the residual vector res with respect to the current model parameters $m = [u; A; B; C]$. The model covariance and Laplacian matrices in Eq. 7 have been separated into the rows that constrain the norm and smoothness of the mean slowness (C_u, L_u) and anisotropic parameters (C_a, L_a) and are weighted by the isotropic (ϵ_u, λ_u) and anisotropic (ϵ_a, λ_a) Lagrangian multipliers. To prevent the solution from favouring anisotropic over isotropic perturbations as the iterations progress, we minimize the cumulative perturbations to f_P (or $f_S^{'}$ when only inverting for S-waves) through the introduction of the sparse (M x M) matrix D_f obtained by differentiating f with respect to A, B, and C at each parameter location current given their current values. The regularisation equations for each parameter set ($\overline{u}$, A, B, and C) are initially scaled by the mean-squared sensitivity to the corresponding parameter. In this way, all regularisation constraints have comparable influence on the objective function prior to the selection of the user-defined Lagrangian multipliers. For all inversion results, we select $\epsilon_u = \epsilon_a = 1$ and $\lambda_u = \lambda_a = 10$ such that isotropic and anisotropic perturbations are equally damped and smoothed. We found these values allow us to adequately fit the data while providing reasonably smooth solutions. The starting reference model is AK135 (Kennett et al., 1995) which closely resembles the far field velocity profile through the geodynamic simulations. The solutions converge after ≤ 3 and ≤ 6 iterations for isotropic and anisotropic inversions, respectively. We refer the reader to (VanderBeek and Faccenda, 2021) and (VanderBeek et al., 2023) for further details on the inversion methodology.

We clarify that arrival times are converted to relative residuals by subtracting the initial 1D model predictions and removing the mean residual for each event. This procedure, known as demeaning, is frequently employed in regional teleseismic tomography to remove the effects of far-field anomalies. The inversion of relative arrival time

residuals provides information only on relative changes in seismic velocity (Aki et al., 1977; Lévêque and Masson, 1999; Masson and Romanowicz, 2017). The consequences of this for resolving anisotropic structure is detailed by VanderBeek & Faccenda (2021). In general, provided the model is sufficiently well-sampled and is anisotropically heterogeneous, then anisotropic fabrics can be accurately recovered.

3. Results

3.1. Geodynamic modeling

In the intraplate hotspot setting model, the plume rises axisymmetrically and subsequently spreads over the Lithosphere-Asthenosphere boundary (LAB) yielding a typical mushroom shape (Fig. 1B). At 30 Ma, the plume tail and head are about 150 km and 1200 km wide, respectively. In the rising plume model, the relatively hotter mantle is characterized by low P- and S-wave isotropic velocity anomalies $\Delta \ln V_{P,S} < -2$ % at the center of the plume head and tail, and radially diminishing (Fig. 2, left column). The S-wave anomalies are slightly more pronounced given their higher sensitivity to temperature. Strong isotropic velocity anomalies are found at the top of the MTZ due to the deepening of the 410 km discontinuity, and at the bottom of the model associated with the source of the plume thermal anomaly. Upper mantle anisotropy up to $2f_P = 9$ %, $2f_S^{''} = 6$ % develops around and within the plume head and tail. The true fast symmetry axes are oriented parallel to the plume conduit and radially at the top and bottom boundaries of the plume head due to the strong component of simple shear deformation. Within the plume head instead, the anisotropy patterns are more complex because of the increasing co-axial deformational component tending to orient the fast symmetry axes tangentially (Ito et al., 2014).

The evolution of the divergent margin model is basically steady-state (time-independent), and it is characterized by the spreading plates causing (i) outgoing lateral flow that is compensated by incoming hot mantle underneath, and (ii) passive mantle upwelling beneath the ridge axis (Fig. 1C). The replacement of the lithosphere with asthenospheric material results in $\Delta \ln V_{P,S} < -4$ % because of the strong contrast in temperature (up to > 1000 K) (Fig. 2, central column). The low velocity anomaly is thicker below the ridge axis and gradually vanishes as the plates thicken. Upper mantle anisotropy develops in the lithosphere and asthenosphere with a maximum $2f_P = 11$ %, $2f_S^{''} = 7$ % found at the LAB. The fast symmetry axes follow the corner flow streamlines, although they tend to dip away from the ridge axis at lithospheric depths. This result is like those of (Kendall et al., 2022; Blackman and Kendall, 2002; Blackman et al., 2017) but differs from those of (Hedjazian et al., 2017) where the fast axes are more horizontal. The reason is that, although similar rheological and micromechanical model parameters have been used, there are differences in the employed boundary conditions and geometry of the numerical domain which result in a different mantle flow and thus velocity gradient and deformational fields.

In the convergent margin model, subduction is initially slow as the slab bends over the top of the lower mantle and continues faster with an average trench retreat rate of ~ 9 cm/yr and slab stagnation in the mantle transition zone (Fig. 1E). The velocity field is characterized by poloidal and toroidal currents that prevail, respectively, at centre and on the side of the subduction zone. The slab is defined by strongly positive isotropic anomalies ($\Delta \ln V_{P,S} > +4$ %) (Fig. 2, right column). Strong anisotropy is present around and within the slab (up to $2f_P = 13$ %, $2f_S^{''} = 9$ %) due to the subduction-induced deformation and the pre-imposed lithospheric fossil fabric. The fast symmetry axes are oriented parallel to slab dip in the entrained mantle and also within the slab (due to a pre-imposed fossil fabric), trench parallel and trench-perpendicular in the subslab and mantle wedge central regions, respectively, and parallel to the toroidal flow field at the plate lateral margins (e.g, Faccenda and Capitano, 2012, 2013).

3.2. Seismic tomography

For each of the three synthetic datasets (Δt_{ISO}, Δt_{HEX} and Δt_{IJ}), we conducted independent P- and S-wave travel-time inversions assuming (i) an isotropic medium, thus neglecting for anisotropy (isotropic inversions; parameter [u]), (ii) an azimuthally anisotropic medium with horizontal fast symmetry axis (azimuthal inversions; parameters [$u; A; B$]), (iii) a tilted symmetry axis transversely isotropic (TTI) medium, thus allowing for a 3D arbitrary orientation of the fast symmetry axes (anisotropic inversions; parameters [$u; A; B; C$]). For the last case, (iv) P- and S-wave delay times were also jointly inverted. In a joint inversion the isotropic velocity fields [$\overline{u}_P, \overline{u}_S$] are left uncoupled. In contrast, coupling between P- and S-waves is intrinsically present in our inversion strategy when updating the anisotropic parameters [$A; B; C$].

The sampling of the imaging volume by P and S waves is shown in Fig. S1 and S2, respectively. The density of sampling is depicted by the derivative weight sum (DWS; Toomey and Foulger, 1989) which provides a reasonable proxy for resolution (Zhang and Thurber, 2007). To convey directional sampling of the medium, we also plot the azimuthal mean resultant length (AMRL; Fisher, 1995; Zhang et al. 2009) defined as $AMRL_j = \sqrt{\left(\left[\sum x_i \right]^2 + \left[\sum y_i \right]^2 \right) \Big/ \sum (x_i^2 + y_i^2)}$ where x_i and y_i are the horizontal ray segment vector components influencing the jth model parameter. In the case of perfect azimuthal sampling, the AMRL = 0 as the different orientations cancel while biased directional sampling yields AMRL near 1. When computing the AMRL for the finite-frequency kernels, the vector components are defined by the azimuth of the nearest ray segment and scaled by the kernel weight. The idealized distribution of seismic sources and receivers considered here results in rather uniform sampling of the medium. Higher DWS is found near the stations where ray paths converge and Fresnel volumes are narrower. Lower AMRL values are found near the center of the array where ray-crossing is greatest.

3.2.1. Plume model

Inversions of isotropic delay times (Δt_{ISO}) are characterized by small low velocity anomalies, which are due to smoothing and vertical smearing effects (Fig. 3). In particular, the relatively thin low-velocity anomaly associated with the plume head disappears almost completely as it gets spread over a thick mantle layer. In anisotropic inversions < 1 % of seismic anisotropy is recovered due to trade-off effects, especially in P-wave maps in correspondence of the plume tail. S-waves better recover the low-velocity anomalies owing to the thinner sensitivity kernels of S-wave compared to P-waves at equivalent dominant periods. Additionally, the slower propagation speeds of shear waves naturally result in larger travel-time delays that drive the inversion.

Inversions of anisotropic delay times (Δt_{IJ}) are shown in Fig. 4. In isotropic inversions, the recovered anomalies are characterized by a strong low velocity anomaly at shallow depths laterally bounded by fast velocity anomalies. At asthenospheric depths one strong (P-wave) or two weaker and converging (S-wave) fast velocity anomalies are present. These anomalies are mainly artifacts resulting from the anisotropy being mapped into isotropic anomalies. Indeed, fast and slow anomalies mainly reflect the vertical and horizontal orientation of the fast symmetry axes, and the effect of the true thermal anomaly is only visible in correspondence of the wide and shallow low velocity anomaly and in the mantle transition zone (S-wave). In the shallow mantle the low-velocity anomaly is surrounded by a broad high-velocity anomaly that can be explained by employed relative arrival-time residuals.

The isotropic anomalies and anisotropic patterns are better recovered in anisotropic, separate or joint, P- and S-wave inversions. S-wave anisotropic inversions yield the best representation of the plume, although again the overall structure is shifted at shallower depths. The velocity anomalies are now attenuated as part of the delay is now
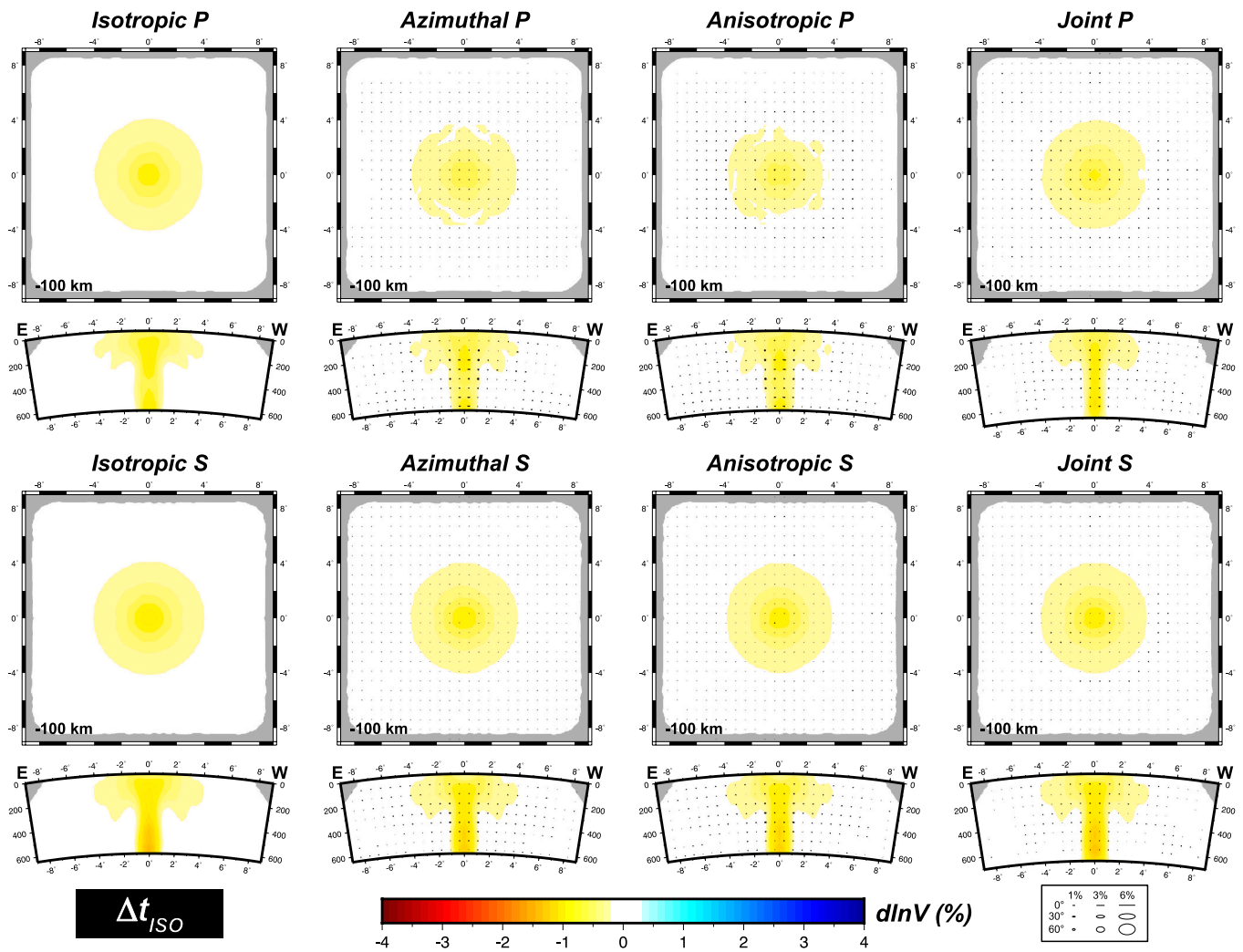
Fig. 3. P-wave (top 2 rows) and S-wave (bottom 2 rows) inversion results of isotropic delay times Δt_{ISO} for the modeled intraplate setting with a rising plume. From left to right columns: isotropic, azimuthal, and anisotropic separate inversions; the last column is for the joint anisotropic inversion. Cross sections with velocity anomalies and ellipses as in Fig. 2.

interpreted as due to seismic anisotropy. The shallow low-velocity anomaly with sub-horizontal fast axes is stronger than in the true model as teleseismic rays are mostly sampling the low-velocity directions. In addition, this anomaly is surrounded by a high-velocity ring with sub-vertical fast symmetry axes. This indicates that in case of relatively strong upper mantle anisotropy, there is a trade-off between isotropic anomalies and anisotropy. This is also observed with the Δt_{HEX} datasets (Fig. S3), indicating that the source of trade-off is not the low-symmetry component of the elastic tensors, but rather in the sub-vertical sampling of the domain by teleseismic rays.

The seismic anisotropy field with the fast symmetry axes that are oriented horizontally within the broad plume head, and vertically along the plume tail is best recovered with the joint P-S inversion. This is because, differently from the uncoupled isotropic velocity fields $[\overline{u}_P, \overline{u}_S]$, the anisotropic parameters [**A**, **B**, **C**] are shared and jointly updated by the P- and S-waves which sample different orientations of the anisotropic media. The azimuthal inversions cannot obviously recover the vertical component of the fast symmetry axes and are contaminated by stronger artifacts relative to anisotropic inversions.

3.2.2. Oceanic spreading ridge model

In all inverse models (Figs. 5, 6, S4) the true low velocity anomaly is not well recovered, and located at sub-lithospheric depths down to the top of the lower mantle because of vertical smearing effects. An

exception is found in inversions of isotropic delay times (Δt_{ISO}) where a strong low velocity anomaly is recovered below the ridge axis (Fig. 5). With increasing plate age this anomaly is gradually replaced by an increasingly thicker high velocity anomaly, while the underlying low-velocity anomaly deepens. Thus, although these recovered features mimic the true age-dependent behavior of the geodynamic model, the location of the isotropic anomalies yields a misleading representation of the mantle thermal structure. This is true especially toward the model lateral boundaries where less data and stations are available.

Inversions of anisotropic delay times (Δt_{IJ}) display similar features, although the isotropic anomalies are stronger due to trade-off effects with anisotropy (Fig. 6). The anisotropic patterns are well recovered in the P-, S- and joint P-S inversions, with the only notable difference being the dipping fast symmetry axes found below the ridge axis having an azimuthal component parallel to it. A fast velocity anomaly is found below the ridge axis in the P-wave inversions, which results from the strong, vertically oriented anisotropy that only the S-waves manage to resolve partially. Similar conclusions can be drawn for the inversions of the Δt_{HEX} datasets (Fig. S4).

3.2.3. Subduction zone model

In inversions of isotropic delay times (Δt_{ISO}) the horizontal portions of the high velocity anomaly associated with the slab are not well recovered (Fig. 7). In P-wave inversions the dipping high velocity
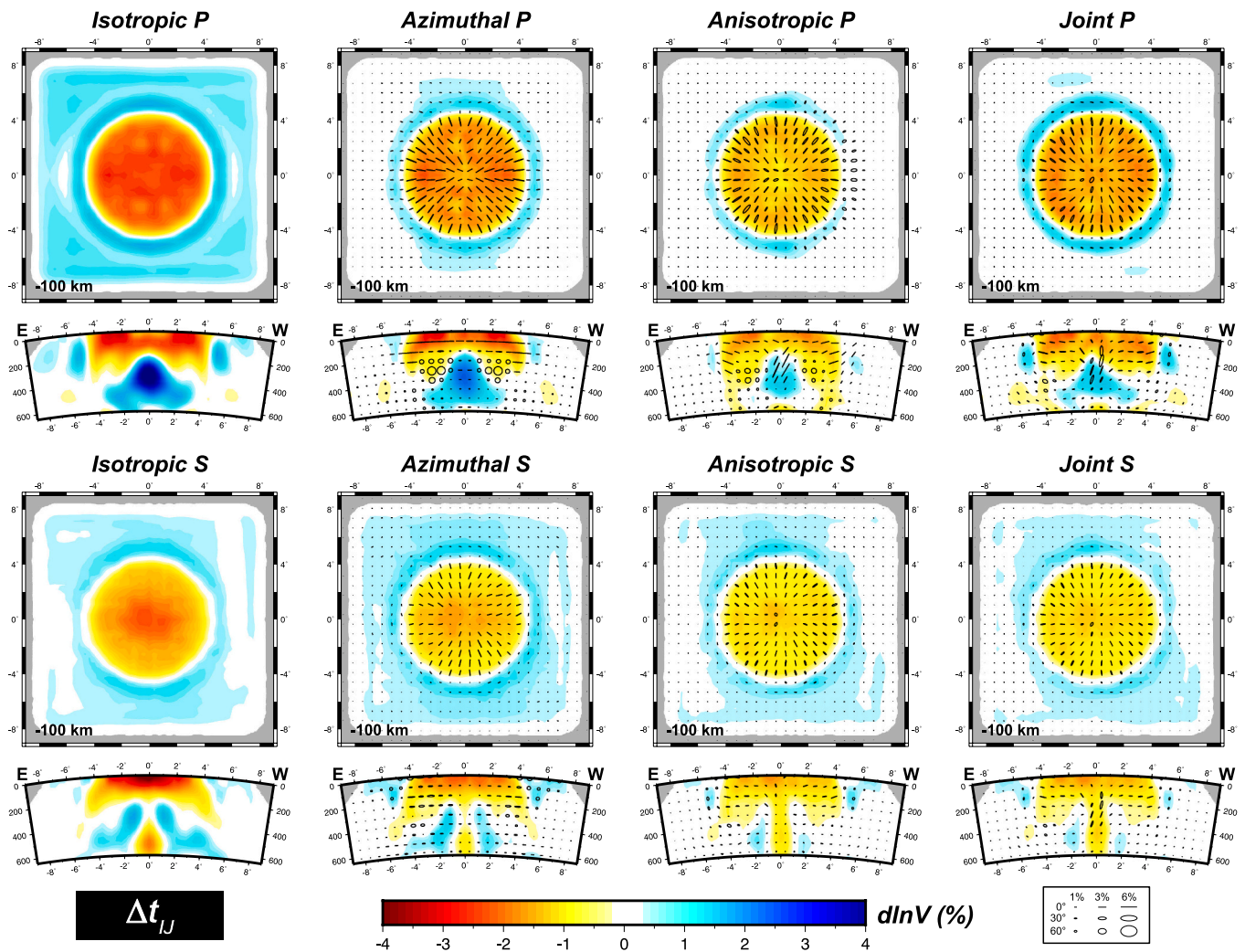
Fig. 4. P-wave (top 2 rows) and S-wave (bottom 2 rows) inversion results of anisotropic delay times Δt_{IJ} for the modeled intraplate setting with a rising plume. From left to right columns: isotropic, azimuthal, and anisotropic separate inversions; the last column is for the joint anisotropic inversion. Cross sections with velocity anomalies and ellipses as in Fig. 2.

anomaly is rather discontinuous, and it fades out when inverting for anisotropy due trade-off effects yielding anisotropic artifacts. These artifacts are also present in S-wave inversions in which, however, the dipping and arcuate portion of the high velocity anomaly is better recovered. The reason for the poor recovery of the fast anomaly geometry in the P-wave inversions is related to its gentle dip which acts to reduce the travel-time delay imparted on near vertically travelling teleseismic waves. S-waves, in contrast, benefit from thinner sensitivity kernels that allows the recovery of relatively thinner anomalies. We note that the synthetic tests of (VanderBeek and Faccenda, 2021) used a subduction model with a steeper dipping slab which allowed for better recovery of the slab anomaly in that study, as well as lower cutoff values for the colorscale (± 2 % against ± 4 %).

Isotropic and azimuthal inversions of anisotropic delay times (Δt_{IJ} and Δt_{HEX}) are contaminated by strong artifacts, especially in the isotropic S-wave inversion where the slab geometry is highly distorted (Fig. 8, S5). The artifacts are stronger than in the rising plume and oceanic spreading models because of the broader and higher in magnitude seismic anisotropy field induced by slab subduction and retreat. The isotropic anomalies artifacts are significantly attenuated when using travel times generated for models with lower amounts of seismic anisotropy (Fig. S6) or in anisotropic inversions. The dipping portion of the fast anomaly is now recovered and better resolved by, respectively, P-wave and S-wave inversions. In anisotropic inversions this is due to

the presence of dipping fossil fabrics within the slab that are sampled along their fast directions and that partly trade-off with velocity anomalies. In the P-wave anisotropic inversions the arcuate geometry of the fast anomaly appears to be discontinuous, which could be misinterpreted as a slab window at its centre. The horizontal fast anomaly in the mantle transition zone is recovered in P-wave model of the joint P-S inversions.

The anisotropic patterns are well recovered by the anisotropic inversions, although (i) anisotropy is present also in the modeled isotropic MTZ because of the vertical smearing and trade-off effects with the isotropic anomalies, and (ii) the strength of the anisotropy is underestimated, especially in the subslab mantle region that appears to be close to isotropic. The toroidal-like pattern of the fast symmetry axes is imaged around the arcuate fast anomaly also by the azimuthal inversion, which however cannot resolve the dipping fabrics close to the dipping fast anomaly and in the mantle wedge.

4. Discussion

4.1. Implications for the recovery of mantle fabrics

The seismic tomography experiments indicate that the employed inverse methodology could be capable of recovering the first order isotropic velocity anomalies and anisotropic patterns in different
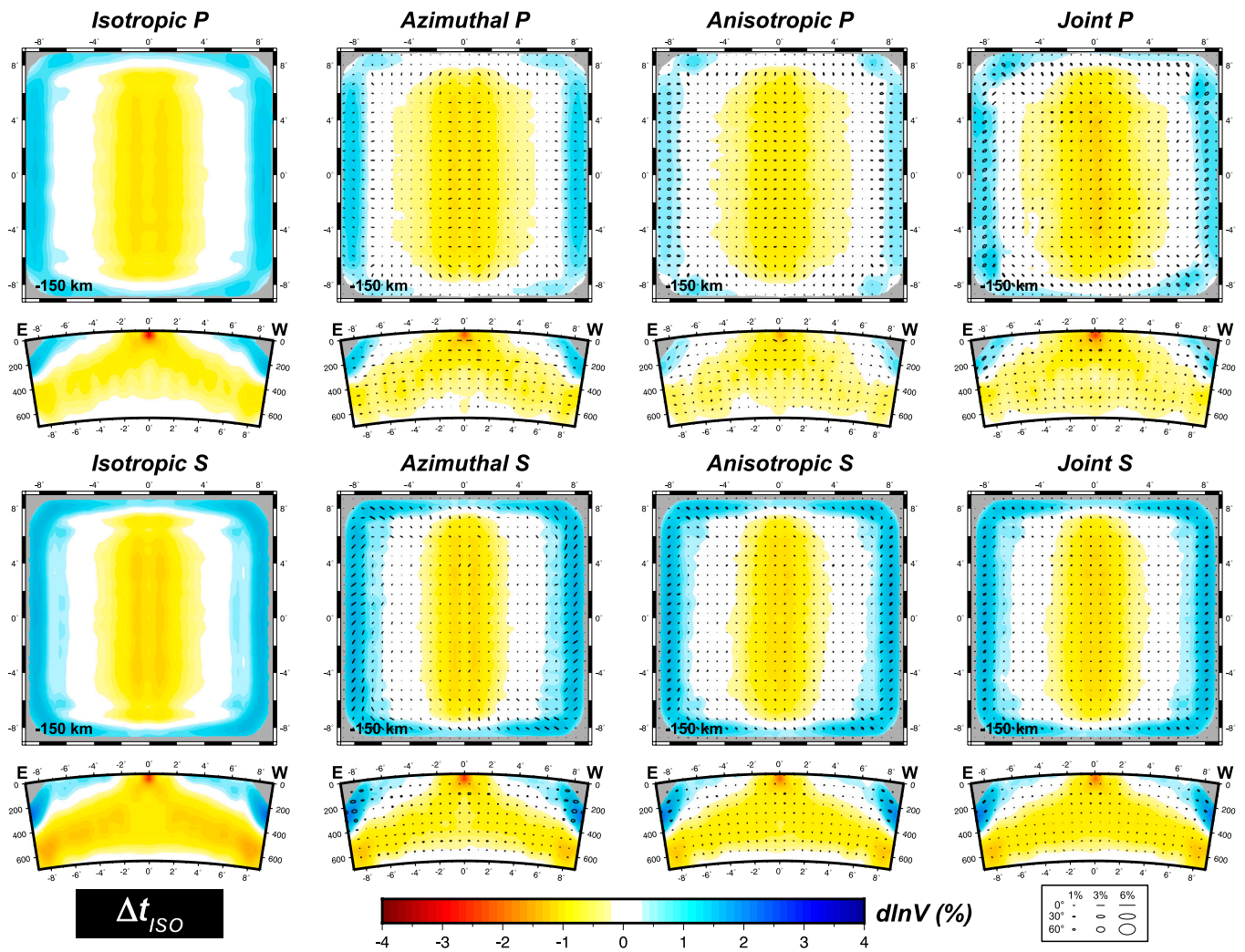
Fig. 5. P-wave (top 2 rows) and S-wave (bottom 2 rows) inversion results of isotropic delay times Δt_{ISO} for the modeled oceanic spreading ridge setting. From left to right columns: isotropic, azimuthal, and anisotropic separate inversions; the last column is for the joint anisotropic inversion. Cross sections with velocity anomalies and ellipses as in Fig. 2.

tectonic settings, with information that shed light on their recent dynamic history and present-day structure. This constitutes a fundamental progress with respect to isotropic body-wave tomographies where seismic anisotropy detected by other independent observations (e.g., surface wave dispersion, SKS splitting, etc.) is not recovered at all and is likely mapped into isotropic artifacts. Yet, the inverse models are strongly affected by vertical smearing due to the high incidence angles of the employed teleseismic phases. Thus, although using an ideal seismic station and azimuthal teleseismic event distribution, more information provided by other seismic waves (i.e., surface waves), or phases (i.e., receiver functions) or different geophysical datasets (i.e., gravity anomalies) is needed to properly recover the Earth's internal structure. Local events can be extremely useful as they illuminate the subduction zone upper mantle from different directions (e.g, Wang and Zhao, 2013). However, it is well established that local deep events occur only at a few convergent margins (Zhang, 2020; Billen, 2020), while other tectonic settings including divergent margins and intra-oceanic hotspots only display shallow seismicity that can be used for imaging crustal structures (Canales et al., 2000). An alternative is adding a-priori constraints about the geometry of tectonic features such as topography of the Moho, LAB, slab interface and thickness (e.g., Zhao et al., 1994), and anisotropic domains (Hammond and Toomey, 2003; Confal et al., 2020; Lee et al., 2021), or confining (squeezing) the anisotropy in some well know layers such as the lithosphere, asthenosphere or the entire

upper mantle (e.g., Hammond and Toomey, 2003; Rappisi et al., 2022). Any of these solutions is likely to improve the recovery of the seismic anomalies and minimize vertical smearing effects.

Anisotropic inversions of isotropic delay times display low degrees of spurious seismic anisotropy (up to $2f = 1$–2 %) which are proportional to the strength of the isotropic anomalies. This indicates that in a weakly anisotropic medium the level of trade-off should be generally quite low. A similar result was obtained in restoration tests when inverting an isotropic model with a real seismic dataset (Rappisi et al., 2022). Conversely, isotropic inversions of anisotropic delay times are contaminated by artifacts whose strength is proportional to the amount of unaccounted for seismic anisotropy (Fig. S6; Bezada et al., 2016; Lee et al., 2021; VanderBeek and Faccenda, 2021; Eddy et al., 2022; VanderBeek et al., 2023). The artifacts are comparable in magnitude to true isotropic anomalies, and therefore constitute a source of strong bias for the geodynamic interpretation in terms of compositional/thermal anomalies and/or petrological processes (i.e., partial melting, subsolidus phase transitions).

Anisotropic inversions of anisotropic delay times are characterized by anisotropic patterns mostly consistent with those of the true models, and by lower magnitude artifacts which are due to the incomplete ray coverage of the anisotropic medium. The S-wave inversions yield the best recovery of the true velocity anomalies and anisotropic patterns because of their higher sensitivity to thermal anomalies and seismic
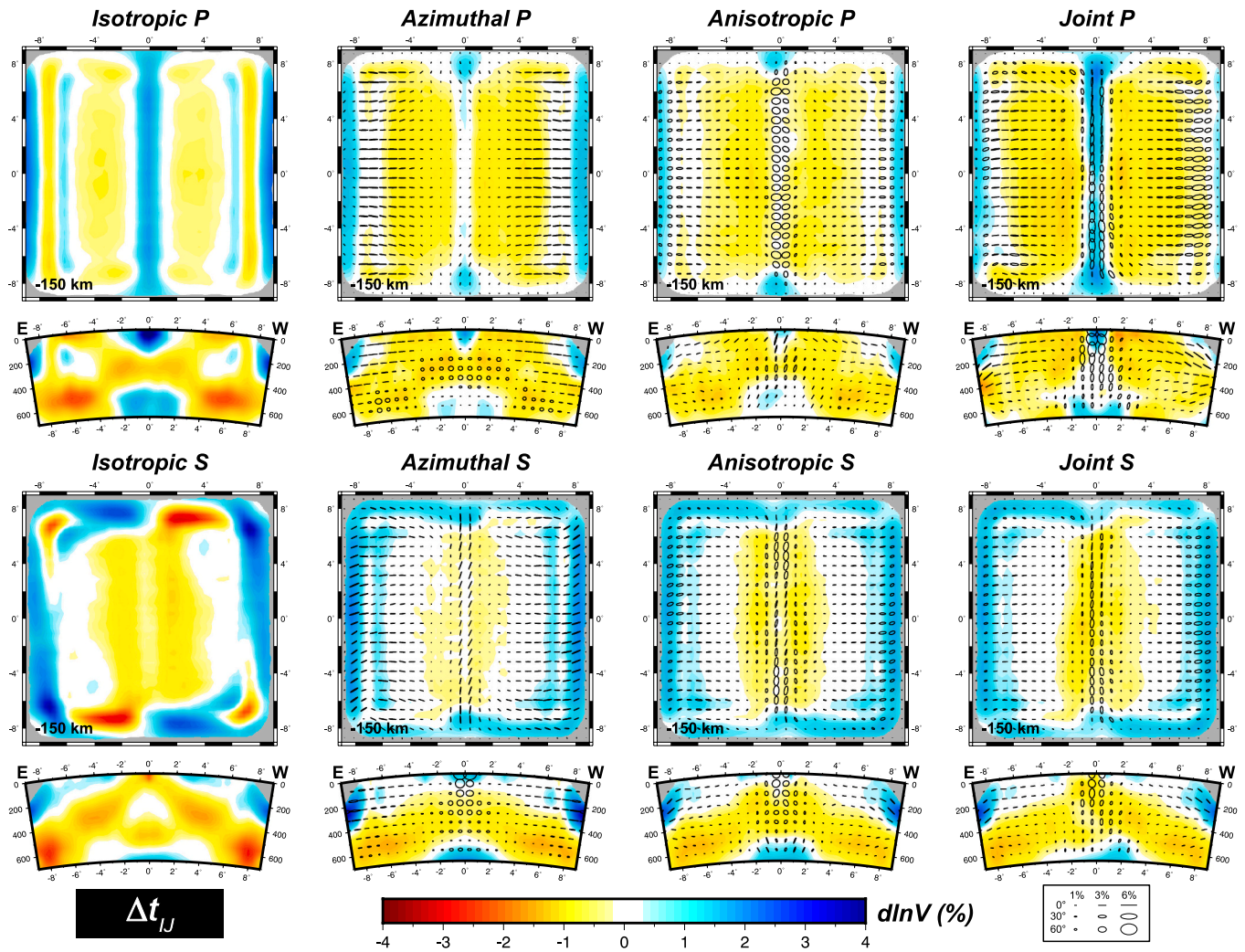
Fig. 6. P-wave (top 2 rows) and S-wave (bottom 2 rows) inversion results of anisotropic delay times **Δt$_{IJ}$** for the modeled oceanic spreading ridge setting. From left to right columns: isotropic, azimuthal, and anisotropic separate inversions; the last column is for the joint anisotropic inversion. Cross sections with velocity anomalies and ellipses as in Fig. 2.

anisotropy, and the tighter sensitivity kernel. Inversions of travel-times computed with the full (**C$_{IJ}$**) or the hexagonally symmetric (**C$_{HEX}$**) tensor fields are almost completely identical. The small differences are due to the higher fraction of total anisotropy present in **C$_{IJ}$** which causes slightly stronger artifacts. This is not surprising when considering that in the modeled upper mantle fabrics the lower-order elastic symmetry components account for < 10 % of the total anisotropy. Naturally-deformed peridotites display hexagonal anisotropy with a fast symmetry axis that account for 50–90 % of the total anisotropy (Browaeys and Chevrot, 2004; Bernard et al., 2021). Consequently, the inversion of teleseismic datasets with the weakly anisotropic hexagonally symmetric medium approximation deserves further testing against more realistic mantle fabrics with a lower hexagonal anisotropy component.

The strength of the velocity anomalies and anisotropy is always underestimated because of vertical smearing and trade-off between isotropic and anisotropic structures, as well as of the applied regularization. The same result has also been obtained in other similar real and synthetic teleseismic datasets studies (e.g., Maguire et al., 2018; Rappisi et al., 2022; Lo Bue et al., 2022), where resolution and restoration tests indicate that, on average, anisotropy is underestimated by 30 % (Rappisi et al., 2022; Lo Bue et al., 2022). A better recovery of the anisotropy magnitude is possible with a more homogeneous seismic ray coverage such as in the upper portion of a seismogenic slab and overlying shallow mantle wedge where anisotropy > 4 % and up to 9 % can be recovered

(Eberhart-Phillips and Reyners, 2009; Wang and Zhao, 2013; Huang et al., 2015; Wang et al., 2022). More generally, however, P-wave azimuthal and radial anisotropy recovered by anisotropy tomographies typically amounts to ≤ 4 % in the hot mantle (e.g., Zhao et al., 2016, 2023; Rappisi et al., 2022). Naturally-deformed peridotites with ≥ 60 % of olivine exhibit P- and S-wave anisotropy of $2f_P \sim 3 - 12$ %, $2f_S \sim 3-8$ % (Mainprice and Silver, 1993; Bernard et al., 2021), which is more consistent with the modelled fabrics (see Section 3.1) than with seismic observations. In addition, it is important to note that, relative to these lithospheric samples, the hot mantle is likely subjected to higher cumulative strains and thus should display higher anisotropy. In conclusion, these considerations suggest that (i) the amount of seismic anisotropy (as well as of isotropic velocity anomalies) present in the mantle is likely higher than the one recovered by anisotropic tomographies, and (ii) laboratory and numerical experiments of high-T creep and fabric evolution in mantle rocks, which have been often criticized of predicting a too high seismic anisotropy, are indeed providing estimates more realistic than is commonly thought.

4.2. Comparison with other teleseismic body-wave tomography experiments

When comparing our results obtained for the three different tectonic settings with other synthetic and real data studies, we note that at the
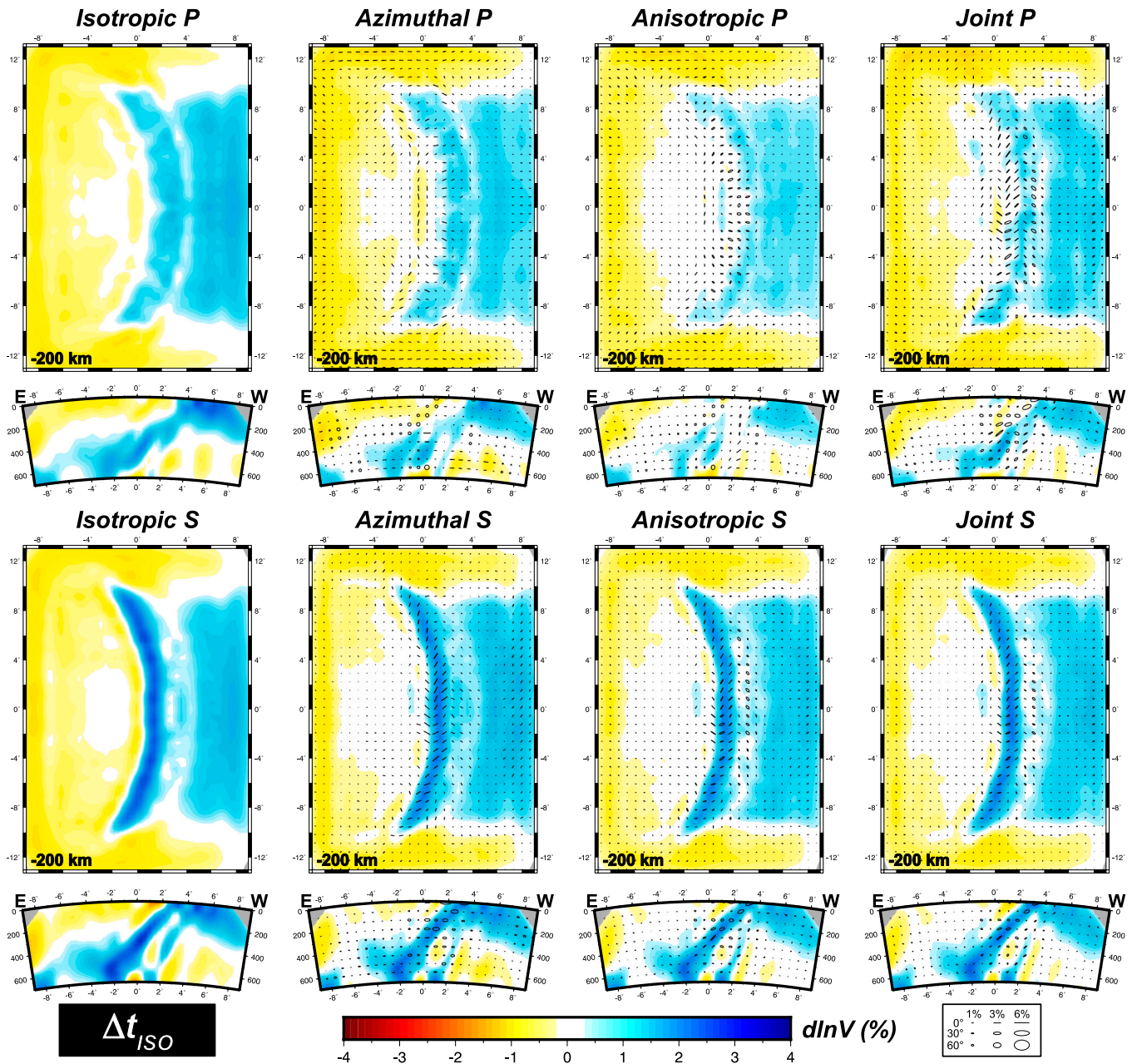
Fig. 7. P-wave (top 2 rows) and S-wave (bottom 2 rows) inversion results of isotropic delay times **Δt$_{ISO}$** for the modeled subduction setting. From left to right columns: isotropic, azimuthal, and anisotropic separate inversions; the last column is for the joint anisotropic inversion. Cross sections with velocity anomalies and ellipses as in Fig. 2.

regional scale most teleseismic anisotropic tomography experiments have been carried out around convergent margins (e.g., Zhao et al., 2016; Wang and Zhao, 2021; Rappisi et al., 2022). This is clearly related to the costly and technically more challenging deployment of regional seismic arrays in oceanic and often remote settings where hotspots and divergent margins are located.

In intraplate hotspot settings, the recovered anisotropic fabrics and velocity anomalies, which define the first-order geometry of the plume tail and head, are better resolved by S-waves due their stronger sensitivity to temperature and narrower Fresnel zone (Figs. 3, 4). Nevertheless, the seismic patterns are underestimated and contaminated by artifacts due to regularization, vertical smearing and trade-off effects. As a result, the plume head is resolved at lithospheric depths, while the plume tail is much thicker than the true one. Similar artifacts were obtained by (Maguire et al., 2018) that carried out isotropic travel-time

tomographies on a geodynamically-derived mantle plume using synthetic teleseismic events and regional arrays. The upper mantle low-velocity anomalies resolved beneath intraplate hotspots by regional teleseismic tomographies are typically $\Delta\ln V_P \sim -0.5$ to 1.5 %, $\Delta\ln V_S \sim -2$ to 4 %, (Suetsugu et al., 2009; Wolfe et al., 2009; Liu and Zhao, 2014; Schlömer et al., 2017; Tsekhmistrenko et al., 2021), i.e., stronger than the ones recovered in our experiments. This can be explained by the presence of (i) partial melting and compositional anomalies (here not modeled), (ii) a more massive and thus more detectable low-velocity body, (iii) a stronger thermal anomaly or body-wave sensitivity to temperature, (iv) different regularization applied in other studies, or (v) by unaccounted for seismic anisotropy generating velocity artifacts. As an example, the high-velocity P-wave anomalies recovered beneath the Tristan mantle plume by (Schlömer et al., 2017) could be explained with vertically-oriented mantle fabrics, while strongly negative velocity
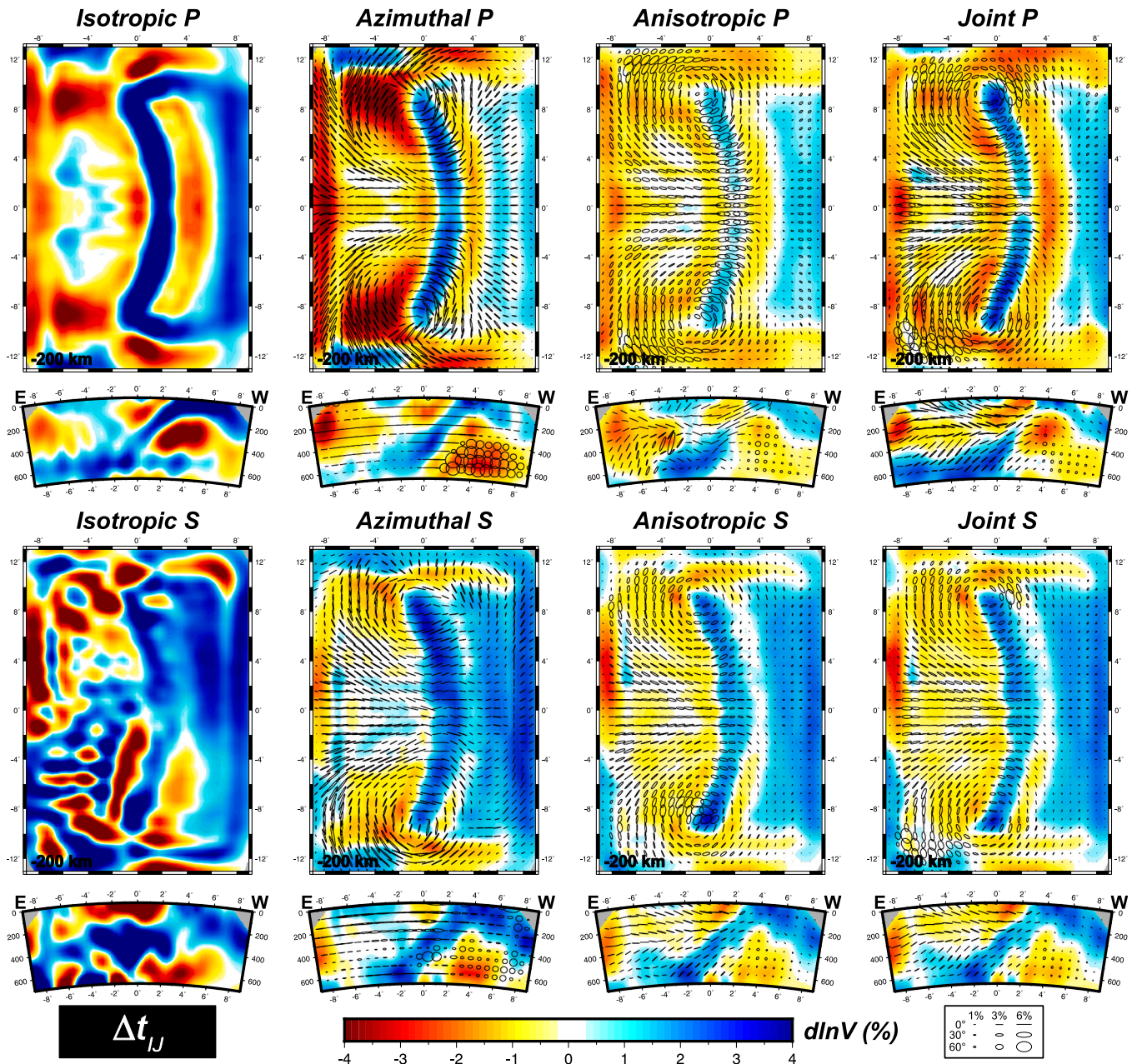
Fig. 8. P-wave (top 2 rows) and S-wave (bottom 2 rows) inversion results of anisotropic delay times **Δt$_{IJ}$** for the modeled subduction setting. From left to right columns: isotropic, azimuthal, and anisotropic separate inversions; the last column is for the joint anisotropic inversion. Cross sections with velocity anomalies and ellipses as in Fig. 2.

anomalies could reflect plume material spreading laterally beneath the lithosphere. With this respect, the recovery of anisotropic patterns can provide precious information about the plume dynamics and the bias generated by potential artifacts.

In the oceanic spreading ridge model, the recovery of the only isotropic, low-velocity anomaly present at lithospheric depths is quite problematic in all inverse models as it is smeared over the entire mantle section (Figs. 5, 6). However, the recovered anisotropic patterns should provide important information about the lithospheric fabrics and asthenosphere dynamics (i.e., symmetric vs. asymmetric, ridge normal vs. oblique upwelling). To our knowledge, the study by (Hammond and Toomey, 2003) is the only one that used teleseismic P- and S-waves in this tectonic setting. In this study, seismic anisotropy is not inverted, but assigned a-priori in uniform domains down to 180 km depth. Furthermore, the model is inverted down to 400 km, which confines the

velocity anomalies in the upper mantle. Yet, the preferred model reported in (Fig. 16d) of (Hammond and Toomey, 2003) shares some similarities with our inversions, in that there is no clear imaging of a thickening high-velocity anomaly corresponding to the diverging oceanic plates. The low-velocity anomaly present beneath the ridge axis is not resolved by our anisotropic inversions because of the strongly anisotropic and vertically-oriented fast axes that trade-off with isotropic velocity anomalies yielding fast (P-wave) or null (S-wave) anomalies. The presence of partial melting (here not modeled) could aid the partial recovery of the low-velocity anomaly.

In teleseismic body wave tomographies carried out at subduction zones the slab is often surrounded by low velocity anomalies like the artifacts that have been imaged in these and other synthetic experiments (Bezada et al., 2016; VanderBeek and Faccenda, 2021; Lo Bue et al., 2022; VanderBeek et al., 2023). The subslab anomalies have been

interpreted as related to either (i) buoyant asthenospheric material accumulating beneath the bending plate (Hawley et al., 2016), (ii) a mantle plume entrained at the base of the upper mantle by the slab (Morishige et al., 2010), (iii) passive upwelling wet mantle transition zone in response to slab retreat (Yang and Faccenda, 2020), (iv) active upwelling of a mantle plume from the lower mantle (Zhao, 2004). Clearly, developing an inversion strategy capable of isolating the true isotropic velocity anomalies, thus yielding un unbiased view of the Earth's interior, is desired before testing all these different scenarios with geodynamic modeling. The supraslab artifacts imaged in the synthetic experiments are particularly concerning as they appear in the mantle wedge where hydrous partial melting is expected according to petrological and thermo-mechanical modelling (e.g., Schmidt and Poli, 1998; Zhao et al., 2007; Gerya, 2011). This implies that, (i) the amount and distribution of mantle wedge partial melting, as well as that of oceanic plate hydration and dehydration, mantle regassing rates, etc., could be erroneously estimated, and (ii), in turn, geodynamic models and laboratory experiments could be wrongly calibrated against these observations. Although velocity artifacts are present in our teleseismic P- and S-wave anisotropic tomographies, their magnitude is substantially reduced. In addition, the highly three-dimensional seismic patterns can be recovered, especially by jointly inverting P and S waves (Fig. 8), allowing to decipher the long-term evolution of the convergent margin.

It is important to note that, besides ignoring seismic anisotropy, other factors can potentially affect the quality of tomographic models. For example, poor ray density and directional coverage limits the resolution of the tomographic solution and allows for greater trade-offs among parameters. A related factor is the acquisition geometry. Here we have considered an idealized distribution of seismic sources and receivers. Despite the optimal coverage of the imaging volume, artefacts are observed in all the models presented and the expression of such artefacts will depend on the sampling of the medium (Bezada et al., 2016). It is also important to acknowledge that regional teleseismic delay time tomography only constrains relative changes in velocity (Aki, 1977; Lévêque and Masson, 1999) which could bias the recovered strength and orientation of anisotropy. The consequences of imaging relative changes in anisotropic velocity are discussed in detail by VanderBeek and Faccenda (2021). In summary, provided the model is sufficiently well-sampled and is anisotropically heterogeneous, then anisotropic fabrics are accurately recovered. Biases arising from inverting relative delay times can readily be investigated through synthetic tests. Additionally, anisotropic imaging results should be validated against absolute measures of anisotropy such as shear wave splitting observations. Ultimately, robustly quantifying these errors requires a stochastic inversion approach capable of exhaustive model space exploration, a direction we are currently investigating (Del Piccolo et al., 2023).

5. Conclusions

In this contribution we have tested the capabilities of a recently developed inverse methodology to simultaneously recover isotropic and anisotropic structures in different tectonic settings. With this respect, we have performed isotropic and anisotropic tomographies of teleseismic P- and S-wave synthetic travel-times generated for geodynamic models of a rising plume in an intraplate setting, a divergent margin characterized by oceanic plate spreading, and a convergent margin with oceanic plate subduction. The anisotropic inversions can capture the main characteristics of the isotropic and anisotropic components of the elastic tensors when accounting for seismic anisotropy. Conversely, in isotropic inversions seismic anisotropy, when present, is mapped into isotropic anomalies, creating artifacts that compromise the geodynamic interpretation of the velocity models. These artifacts are undistinguishable from real velocity anomalies and therefore are likely to bias the interpretation of the tectonic setting structure and dynamics. In azimuthal

inversions the horizontal component of sub-horizontal fast symmetry axes is generally well recovered, while isotropic artifacts appear in correspondence of sub-vertical fabrics.

Vertical smearing affects all the inverse models due to the high-incidence angles of the teleseismic phases. Because of the paucity and shallowness of the local seismicity in many regional tectonic settings and considering the computationally demanding nature of the full-waveform inversion, jointly inverting body wave with surface wave derived observables and/or other geophysical datasets provides another avenue for improving resolution of tomographic models. As an example, (Yuan et al., 2011) have combined surface waves and SKS splitting data to develop a 3-D upper mantle model of North America that includes isotropic shear velocity and radial and azimuthal anisotropy. Another dataset that can be considered to further constrain the anisotropy is the shear waves splitting intensity, given that its primarily sensitive to seismic anisotropy and not isotropic structure (VanderBeek et al., 2023).

CRediT authorship contribution statement

VanderBeek Brandon Paul: Writing – review & editing, Software, Methodology, Conceptualization. **Faccenda Manuele:** Writing – original draft, Visualization, Software, Project administration, Funding acquisition, Conceptualization.

Declaration of Competing Interest

The authors declare the following financial interests/personal relationships which may be considered as potential competing interests: Manuele Faccenda reports financial support was provided by European Research Council.

Data availability

Data will be made available on request.

Appendix A. Supporting information

Supplementary data associated with this article can be found in the online version at doi:10.1016/j.jog.2023.102003.

References

Aki, K., Christoffersson, A., Husebye, E.S., 1977. Determination of the three- dimensional seismic structure of the lithosphere. J. Geophys. Res. 82 (2), 277–296.

Aster, R.C., Borchers, B., Thurber, C.H., 2018. Parameter estimation and inverse problems. Elsevier.

Babuška, V., Cara, M., 1991. Seismic anisotropy in the Earth. Kluwer Academic Publishers, Dordrecht, pp. 1–217.

Becker, T.W., Chevrot, S., Schulte-Pelkum, V., Blackman, D.K., 2006. Statistical properties of seismic anisotropy predicted by upper mantle geodynamic models. J. Geophys. Res. 111 (B8), B08309 https://doi.org/10.1029/2005JB004095.

Bernard, R.E., Schulte-Pelkum, V., Behr, W.M., 2021. The competing effects of olivine and orthopyroxene CPO on seismic anisotropy. Tectonophys 814, 228954.

Bezada, M., Faccenda, M., Toomey, D.R., 2016. Representing anisotropic subduction zones with isotropic velocity models: a characterization of the problem and some steps on a possible path forward. Geochem. Geophys. Geosyst. https://doi.org/10.1002/2016GC006507.

Billen, M.I., 2020. Deep slab seismicity limited by rate of deformation in the transition zone. Sci. Adv. 6 (22) https://doi.org/10.1126/sciadv.aaz7692.

Blackman, D.K., Boyce, D.E., Castelnau, O., Dawson, P.R., Laske, G., 2017. Effects of crystal preferred orientation on upper-mantle flow near plate boundaries: rheologic feedbacks and seismic anisotropy. Geophys. J. Int. 210, 1481–1493.

Blackman, D.K., Kendall, J.-M., 2002. Seismic anisotropy in the upper mantle, 2, Predictions for current plate boundary flow models. Geochem. Geophys. Geosyst. 3 (9), 8602. https://doi.org/10.1029/2001GC000247.

Bokelmann, G.H., 2002. Convection-driven motion of the North American craton: evidence from P-wave anisotropy. J. Geophys. Int. 148 (2), 278–287.

Boneh, Y., Morales, L.F.G., Kaminski, E., Skemer, P., 2015. Modeling olivine CPO evolution with complex deformation histories: Implications for the interpretation of seismic anisotropy in the mantle. Geochem. Geophys. Geosyst. 16, 3436–3455. https://doi.org/10.1002/2015GC005964.

Browaeys, J.T., Chevrot, S., 2004. Decomposition of the elastic tensor and geophysical applications. Geophys. J. Int. 159 (2), 667–678.

Burov, E., Gerya, T.V., 2014. Asymmetric three-dimensional topography over mantle plumes. Nature 513, 85–89.

Canales, J.P., Detrick, R.S., Lin, J., Collins, J.A., Toomey, D.R., 2000. Crustal and upper mantle seismicstructure beneath the rift mountains and across a nontransform offset at the Mid-Atlantic Ridge (35°N). J. Geophys. Res. 105, 2699–2719.

Chang, S.-J., Ferreira, A.M.G., Faccenda, M., 2016. Upper- and mid-mantle interaction between the Samoan plume and the Tonga-Kermadec slabs. Nat. Commun. 7, 10799 https://doi.org/10.1038/ncomms10799.

Chevrot, S., Favier, N., Komatitsch, D., 2004. Shear wave splitting in three-dimensional anisotropic media. Geophys. J. Int. 159 (2), 711–720.

Chust, T.C., Steinle-Neumann, G., Dolejs, D., Schuberth, B.S., Bunge, H.P., 2017. MMA-EoS: a computational framework for mineralogical thermodynamics. J. Geophys. Res. 122, 9881–9920.

Colli, L., Ghelichkhan, S., Bunge, H.-P., 2016. On the ratio of dynamic topography and gravity anomalies in a dynamic Earth. Geophys. Res. Lett. 43, 2510–2516. https://doi.org/10.1002/2016GL067929.

Confal, J.M., Bezada, M.J., Eken, T., Faccenda, M., Saygin, E., Taymaz, T., 2020. Influence of upper mantle anisotropy on isotropic P-wave tomography images obtained in the Eastern Mediterranean region. J. Geophys. Res. 125 (8) https://doi.org/10.1029/2019JB018559.

Crotwell, H.P., Owens, T.J., Ritsema, J., 1999. The TauP Toolkit: flexible seismic traveltime and ray-path utilities. Seismol. Res. Lett. 70 (2), 154–160.

Dahlen, F.A., Hung, S.H., Nolet, G., 2000. Fréchet kernels for finite- frequency traveltimes–I. Theory. J. Geophys. Int. 141 (1), 157–174.

Eberhart-Phillips, D., Reyners, M., 2009. Three-dimensional distribution of seismic anisotropy in the Hikurangi subduction zone beneath the central North Island, New Zealand. J. Geophys. Res. 114, B06301 https://doi.org/10.1029/2008JB005947.

Eddy, C.L., Ekström, G., Nettles, M., 2022. Three-dimensional seismic anisotropy in the Pacific upper mantle from inversion of a surface-wave dispersion dataset. Geophys. J. Int. 231, 355–383.

Faccenda, M., Capitanio, F.A., 2012. Development of mantle seismic anisotropy during subduction-induced 3D flow. Geophys. Res. Lett. 39 https://doi.org/10.1029/2012GL051988.

Faccenda, M., Capitanio, F.A., 2013. Seismic anisotropy around subduction zones: insights from three-dimensional modeling of upper mantle deformation and SKS splitting calculations. Geochem. Geophys. Geosyst. https://doi.org/10.1002/ggge.20055.

Faccenda, M., 2014. Mid mantle seismic anisotropy around subduction zones. Phys. Earth Planet. Int. 227, 1–19.

Faccenda, M., VanderBeek, B., de Montserrat, A., 2021. ECOMAN: a new open source software for Exploring the Consequences of Mechanical Anisotropy in the maNtle. EGU General Assembly.

Fisher, N.I., 1995. Statistical Analysis of Circular Data. Cambridge Univ. Press.

Gerya, T., 2011. Future directions in subduction modeling. J. Geodyn. 52 (5), 344–378. https://doi.org/10.1016/j.jog.2011.06.005.

Gerya, T., 2019. Introduction to numerical geodynamic modelling. Cambridge University Press.

Gresillaud, A., Cara, M., 1996. Anisotropy and P-wave tomography: a new approach for inverting teleseismic data from a dense array of stations. Geophys. J. Int. 26, 77–91.

Hammond, W.C., Toomey, D.R., 2003. Seismic velocity anisotropy and heterogeneity beneath the Mantle Electromagnetic and Tomography Experiment (MELT) region of the East Pacific Rise from analysis of P and S body waves. J. Geophys. Res. 108 (B4) https://doi.org/10.1029/2002JB001789.

Hawley, W.B., Allen, R.M., Richards, M.A., 2016. Tomography reveals buoyant asthenosphere accumulating beneath the Juan de Fuca plate. Science 353, 1406–1408.

Hedjazian, N., Garel, F., Rhodri Davies, D., Kaminski, 2017. Age-independent seismic anisotropy under oceanic plates explained by strain history in the asthenosphere. Earth Planet. Sci. Lett. 460, 135–142.

Huang, Z., Zhao, D., Liu, X., 2015. On the trade-off between seismicanisotropy and heterogeneity: numericals imulations and application to Northeast Japan. J. Geophys. Res. 120, 3255–3277. https://doi.org/10.1002/2014JB011784.

Hu, J., Faccenda, M., Liu, L., 2017. Subduction-controlled mantle flow and seismic anisotropy in South America. Earth Planet. Sci. Lett. 470, 13–24. https://doi.org/10.1016/j.epsl.2017.04.027.

Ito, G., Dunn, R., Li, A., Wolfe, C.J., Gallego, A., Fu, Y., 2014. Seismic anisotropy and shear wave splitting associated with mantle plume-plate interaction. J. Geophys. Res. 119, 4923–4937. https://doi.org/10.1002/2013JB010735.

Kaminski, E., Ribe, N.M., Browaeys, J.T., 2004. D-Rex, a program for calculation of seismic anisotropy due to crystal lattice preferred orientation in the convective upper mantle. Geophys. J. Int. 158 (2), 744–752. https://doi.org/10.1111/j.1365-246x.2004.02308.x.

Karato, S.-I., Wu, P., 1993. Rheology of the upper mantle: A synthesis. Science 260 (5109), 771–778. https://doi.org/10.1126/science.260.5109.771.

Katayama, I., Karato, S.-I., 2008. Low-temperature, high-stress deformation of olivine under water-saturated conditions. Phys. Earth Planet. Int. 168, 125–133. https://doi.org/10.1016/j.pepi.2008.05.019.

Katz, R.F., Knepley, M.G., Smith, B., Spiegelman, M., coon, E.T., 2007. Numerical simulation of geodynamic processes with the Portable Extensible Toolkit for scientific computation. Phyis. Earth Planet. Int. 163, 52–68.

Kendall, E., Faccenda, M., Ferreira, A.M.G., Chang, S.-J., 2022. On the relationship between oceanic plate speed, tectonic stress, and seismic anisotropy. Geophys. Res. Lett. 49, e2022GL097795 https://doi.org/10.1029/2022GL097795.

Kennett, B.L., Engdahl, E.R., Buland, R., 1995. Constraints on seismic velocities in the Earth from traveltimes. Geophys. J. Int. 122 (1), 108–124.

Lee, H., Bezada, M.J., Faccenda, M., 2021. Can sub-slab low-velocity anomalies be an artifact caused by anisotropy? A case study from the Alboran slab area in the western Mediterranean. Tectonophys 819, 229080.

Lévêque, J.J., Masson, F., 1999. From ACH tomographic models to absolute velocity models. Geophys. J. Int. 137 (3), 621–629.

Liu, X., Zhao, D., 2014. Seismic evidence for a mantle plume beneath the Cape Verde hotspot. Int. Geol. Rev. 56 (10), 1213–1225.

Lo Bue, R., Faccenda, M., Yang, J., 2021. The role of Adria Plate Lithospheric Structures on the Recent Dynamics of the Central Mediterranean Region. J. Geophys. Res. 126, e2021JB022377 https://doi.org/10.1029/2021JB022377.

Lo Bue, R., Rappisi, F., VanderBeek, B.P., Faccenda, M., 2022. Tomographic image interpretation and central-western Mediterranean-like upper mantle dynamics from coupled seismological and geodynamic modeling approach. Front. Earth Sci. 10, 884100 https://doi.org/10.3389/feart.2022.884100.

Long, M.D., Becker, T.W., 2010. Mantle dynmics and seismic anisotropy. Earth Planet. Sci. Lett. 297.

Maguire, R., Ritsema, J., Bonnin, M., van Keken, P.E., Goes, S., 2018. Evaluating the resolution of deep mantle plumes in teleseismic traveltime tomography. J. Geophys. Res. 123, 384–400. https://doi.org/10.1002/2017JB014730.

Mainprice, D., Silver, P.G., 1993. Interpretation of SKS-waves using samples from the subcontinental lithosphere. Phys. Earth Planet. Inter. 78 (3–4), 257–280.

Masson, Y., Romanowicz, B., 2017. Box tomography: localized imaging of remote targets buried in an unknown medium, a step forward for understanding key structures in the deep Earth. Geophys. J. Int. 211 (1), 141–163.

McNamara, A.K., van Keken, P.E., Karato, S.-I., 2002. Development of anisotropic structure in the Earth's lower mantle by solid-state convection. Nature 416, 310–314.

Mishin, Y.A., Gerya, T.V., Burg, J.-P., Connolly, J.A., 2008. Dynamics of double subduction: numerical modeling. Phys. Earth Planet. Inter. 171 (1–4), 280–295. https://doi.org/10.1016/j.pepi.2008.06.012.

Montagner, J.P., 1998. Where can seismic anisotropy be detected in the Earth's mantle? In boundary layers…. Pure Appl. Geophys. 151, 223–256.

Morishige, M., Honda, S., Yoshida, M., 2010. Possibility of hot anomaly in the sub-slab mantle as an origin of low seismic velocity anomaly under the subducting Pacific plate. Phys. Earth Planet. Int. 183, 353–365.

Morra, G., Regenauer-Lieb, K., Giardini, D., 2006. Curvature of oceanic arcs. Geology 34 (10), 877–880.

Munzarová, H., Plomerová, J., Kissling, E., 2018. Novel anisotropic teleseismic body-wave tomography code AniTomo to illuminate heterogeneous anisotropic upper mantle: Part I–theory and inversion tuning with realistic synthetic data. Geophys. J. Int. 215 (1), 524–545.

Nolet, A., Allen, R., Zhao, D., 2007. Mantle plume tomography. Chem. Geol. 241, 248–263.

Paige, C.C., Saunders, M.A., 1982. LSQR: An algorithm for sparse linear equations and sparse least squares. ACM Trans. Math. Softw. (TOMS) 8 (1), 43–71.

Del Piccolo, G., VanderBeek, B., Faccenda, M., Morelli, A., Byrnes, J. (2023). Reversible-Jump, Markov-Chain Monte Carlo seismic tomographic inversion for anisotropic structure in subduction zones (No. EGU23–9927). Copernicus Meetings.

Plomerová, J., Babuška, V., 2010. Long memory of mantle lithosphere fabric - European LAB constrained from seismic anisotropy. Lithos 120, 131–143.

Plomerová, J., Vecsey, L., Babuška, V., 2012. Mapping seismic anisotropy of the lithospheric mantle beneath the northern and eastern Bohemian Massif (central Europe). Tectonophys 564–565, 38–53.

Rappisi, F., VanderBeek, B.P., Faccenda, M., Morelli, A., Molinari, I., 2022. Slab geometry and upper mantle flow patterns in the Central Mediterranean from 3D anisotropic P-wave tomography. J. Geophys. Res. 127, e2021JB023488. ⟨https://doi.rg/10/2021JB023488⟩.

Rümpker, G., Silver, P.G., 1998. Apparent shear-wave splitting parameters in the presence of vertically varying anisotropy. Geophys. J. Int. 135 (3), 790–800.

Schlömer, A., Geissler, W.H., Jokat, W., Jege, M., 2017. Hunting for the Tristan mantle plume – An upper mantle tomography around the volcanic island of Tristan da Cunha. Earth Planet. Sci. Lett. 462, 122–131.

Schmandt, B., Humphreys, E., 2010. Seismic heterogeneity and small- scale convection in the southern California upper mantle. Geochem. Geophys. Geosyst 11 (5) https://doi.org/10.1029/2010GC003042.

Schmidt, M.W., Poli, S., 1998. Experimentally based water budgets for dehydrating slabs and consequences for arc magma generation. Earth Planet. Sci. Lett. 163, 361–379.

Schulte-Pelkum, V., Blackman, D.K., 2003. A synthesis of seismic P and S anisotropy. J. Geophys. Int 154 (1), 166–178.

Sieminski, A., Liu, Q., Trampert, J., Tromp, J., 2007. Finite-frequency sensitivity of body waves to anisotropy based upon adjoint methods. J. Geophys. Int 171 (1), 368–389.

Silver, P.G., Chan, W.W., 1991. Shear wave splitting and subcontinental mantle deformation. J. Geophys. Res.: Solid Earth 96 (B10), 16429–16454.

Stixrude, L., Lithgow-Bertelloni, C., 2011. Thermodynamics of mantle minerals: II. Phase equilibria. Geophys. J. Int. 184 (3), 1180–1213.

Sturgeon, W., Ferreira, A.M.G., Faccenda, M., Chang, S.-J., Schardong, L., 2019. On the origin of radial anisotropy near subducted slabs in the midmantle. Geochem. Geophys. Geosys. 20 (11), 5105–5125. https://doi.org/10.1029/2019GC008462.

Suetsugu, D., Isse, T., Tanaka, S., Obayashi, M., Shiobara, H., Sugioka, H., Kanazawa, T., Fukao, Y., Barruol, G., Reymond, D., 2009. South Pacific mantle plumes imaged by seismic observation on islands and seafloor. Geochem. Geophys. Geosyst. 10, Q11014 https://doi.org/10.1029/2009GC002533.

Tarantola, A., Valette, G., 1982. Generalized nonlinear inverse problems solved using the least squares criterion. Rev. Geophys. 20 (2), 219–232.

Thomsen, L., 1986. Weak elastic anisotropy. Geophysics 51 (10), 1954–1966.

Tommasi, A., Vauchez, A., 2015. Heterogeneity and anisotropy in the lithospheric mantle. Tectonophys 661, 11–37.

Toomey, D.R., Foulger, G.R., 1989. Tomographic inversion of local earth- quake data from the Hengill-Grensdalur central volcano complex, Iceland. J. Geophys. Res. 94 (B12), 17497–17510.

Tsekhmistrenko, M., Sigloch, K., Hosseini, K., Barroul, G., 2021. A tree of Indo-African mantle plumes imaged by seismic tomography. Nat. Geo. 14, 612–619.

Turcotte, D., Schubert, G., 2014. Geodynamics, Vol. 160–228. Cambridge University Press,, pp. 263–334.

VanderBeek, B.P., Faccenda, M., 2021. Imaging upper mantle anisotropy with teleseismic *P*-wave delays: insights from tomographic reconstructions of subduction simulations. Geophys. J. Int. 225, 2097–2119.

VanderBeek, B.P., Lo Bue, R., Rappisi, F., and Faccenda, M., 2023. Imaging upper mantle anisotropy with travel-time and splitting intensity observations from teleseismic shear waves: Insights from tomographic reconstructions of subduction simulations. https://doi.org/10.1093/gji/ggad389.

Vinnik, L.P., Kind, R., Kosarev, G.L., Makeyeva, L.I., 1989. Azimuthal anisotropy in the lithosphere from observations of long-period S-waves. Geophys. J. Int. 99 (3), 549–559.

Wang, J., Zhao, D., 2013. P-wave tomography for 3-D radial and azimuthal anisotropy of Tohoku and Kyushu subduction zones. Geophys. J. Int. 193 (3), 1166–1181.

Wang, Z., Zhao, D., 2021. 3D anisotropic structure of the Japan subduction zone. Sci. Adv. 7, eabc9620.

Wang, Z., Zhao, D., Chen, X., 2022. Seismic anisotropy and intraslab hydrated faults beneath the NE Japan forearc. Geophy. Res. Lett. 49 e2021GL097266.

Wolfe, C.J., et al., 2009. Mantle Shear-Wave Velocity Structure Beneath the Hawaiian Hot Spot. Science 326, 1388–1390.

Wu, H., Lees, J.M., 1999. Cartesian parametrization of anisotropic traveltime tomography. Geophys. J. Int. 137, 64–80.

Yang, J., Faccenda, M., 2020. Intraplate volcanism originating from upwelling hydrous transition zone (-). Nature 579, 88–91. https://doi.org/10.1038/s41586-020-2045-y.

Yuan, H., Romanowicz, B., Fisher, K.M., Abt, D., 2011. 3-D shear wave radially and azimuthally anisotropic velocity model of the North American upper mantle. Geophys. J. Int. 184 (3), 1237–1260.

Zhang, H., Thurber, C.H., 2007. Estimating the model resolution matrix for large seismic tomography problems based on Lanczos bidiagonalization with partial reorthogonalization. J. Geophys. Int 170 (1), 337–345.

Zhang, H., Thurber, C., Bedrosian, P., 2009. Joint inversion for Vp, Vs, and Vp/Vs at SAFOD, Parkfield, California. Geochem. Geophys. Geosyst. 10 (11) https://doi.org/10.1029/2009GC002709.

Zhang, Z., 2020. Mechanisms and implications of deep earthquakes. Ann. Rev. Earth Planet. Sci. Vol. 48, 147–174.

Zhao, D., Hasegawa, A., Kanamori, H., 1994. Deep structure of Japan subduction zone as derived from local, regional, and teleseismic events. J. Geophys. Res. 99, 22313–22329.

Zhao, D., 2004. Global tomographic images of mantle plumes and subducting slabs: insight into deep Earth dynamics. Phys. Earth Planet. Int. 146, 3–34.

Zhao, D., Liu, X., Wang, Z., Gou, T., 2023. Seismic anisotropy tomography and mantle dynamics. Surv. Geophys. https://doi.org/10.1007/s10712-022-09764-7.

Zhao, D., Maruyama, S., Omori, S., 2007. Mantle dynamics of Western Pacific and East Asia: insight from seismic tomography and mineral physics. Gond. Res. 11, 120–131.

Zhao, D., Yu, S., Liu, X., 2016. Seismic anisotropy tomography: new insight into subduction dynamics. Gondwana Res. 33, 24–43.

Zhou, Q., Hu, J., Liu, L., Chaparro, T., Stegman, D.R., Faccenda, M., 2018. Western U.S. seismic anisotropy revealing complex mantle dynamics. Earth Planet. Sci. Lett. 500, 156–167. https://doi.org/10.1016/j.epsl.2018.08.015.